CHALMERS
UNIVERSITY OF TECHNOLOGY

Perovskite redox materials for renewable hydrogen generation

Exploration and synthesis of perovskite-type oxides for Chemical Looping applications

Master's thesis 2026

ÀLEX FUENTES RUIZ

DEPARTMENT OF SPACE, EARTH AND ENVIRONMENT
CHALMERS UNIVERSITY OF TECHNOLOGY

Gothenburg, Sweden 2026
www.chalmers.se

MASTER'S THESIS 2026

Perovskite redox materials for renewable hydrogen generation

Exploration and synthesis of perovskite-type oxides for Chemical Looping applications

ÀLEX FUENTES RUIZ

CHALMERS
UNIVERSITY OF TECHNOLOGY

Department of Space, Earth and Environment
Division of Energy Technology
CHALMERS UNIVERSITY OF TECHNOLOGY
Göteborg, Sweden 2026

Perovskite redox materials for renewable hydrogen generation

Master's Thesis 2026

Department of Space, Earth and Environment
Division of Energy Technology
Chalmers University of Technology
SE-41296 Göteborg
Sweden

Tel. +34 617142797

Department of Space, Earth and Environment
Göteborg, Sweden 2026

Perovskite redox materials for renewable hydrogen generation

ÀLEX FUENTES RUIZ
Department of Space, Earth and Environment
Division of Energy Technology
Chalmers University of Technology

Abstract

The transition towards sustainable energy systems necessitates the development of efficient methods for green hydrogen production. This master's thesis investigates the potential of perovskite-type oxides ($ABO_{3-\delta}$) as oxygen carriers for Chemical Looping systems, specifically for hydrogen generation via the Steam-Iron Process (SIP). Unlike traditional iron oxides, perovskites offer a flexible structure that allows for the tuning of redox properties and thermal stability through ionic substitution. The master thesis focuses on the synthesis and characterization of a series of perovskites based on calcium (Ca), lanthanum (La), iron (Fe), and manganese (Mn). A reproducible synthesis methodology was established to prepare 13 samples with different compositions and stoichiometries between them. The structural integrity and phase purity of the synthesized materials were evaluated using X-ray Diffraction (XRD), while the oxygen exchange capacity and redox kinetics were analysed via Thermogravimetric Analysis (TGA) under isothermal reduction and oxidation cycles with CO and CO_2, respectively, at 800 °C. XRD results confirmed that manganate-based perovskites, such as $CaMnO_3$ and $LaMnO_3$, achieved high structural fidelity, whereas pure ferrites exhibited incomplete stabilization and the presence of secondary phases. TGA revealed that iron-containing structures demonstrate a higher capacity for oxygen release (vacancy formation) but lower thermal stability. Conversely, calcium substitution at the A-site enhanced thermal stability but was found to reduce reaction kinetics in certain compositions. The primary conclusion of this study identifies Sample 4 ($LaFeO_3$) and Sample 13 ($Ca_{0.5}La_{0.5}FeO_{3-\delta}$) as the most promising candidates. These specific compositions demonstrated a synergistic effect between iron, lanthanum and calcium, outperforming other compounds due to its exceptional CO_2 splitting performance (high Oxygen Exchange Capacity) and rapid oxidation kinetics, validating its suitability for continuous hydrogen production in fluidized bed systems.

Keywords: Oxygen carrier, circulating fluidized bed, perovskite, hydrogen production, steam-iron process, chemical looping, oxygen exchange capacity, XRD, TGA

Acknowledgements

First of all, I want to thank my family for their unconditional support throughout my time as a graduate student and during the completion of this project. I deeply appreciate his constant presence and his encouragement have been instrumental in this stage.

To my partner, for his endless patience and support especially in the most difficult moments. His understanding, constant encouragement and presence have been a source of strength and continuous inspiration throughout.

Finally, I would like to express my gratitude to my project supervisor Ivana Stanicic and the examiner Magnus Rydén for his guidance, patience and wisdom throughout this Master Thesis. Thank you for sharing your knowledge, for inspiring me to constantly improve, and for giving me the tools I need to achieve academic success.

Contents

List of Figures

List of Tables

1. Introduction

1.1. Climate change and CO_2 emissions

There is currently a strong scientific consensus that human activities are the primary driver of global warming, phenomenon largely driven by the emission of greenhouse gases, with carbon dioxide (CO_2) being the single largest contributor. The primary sources of these emissions are the combustion of fossil fuels, which account for approximately 80% of global emissions [1]. Atmospheric CO_2 concentrations have reached levels not seen in at least two million years, driving a global surface temperature increase of 1.1 °C above pre-industrial levels [2].

To adhere to the Paris Agreement and limit global warming to 1.5°C achieving net zero emissions by 2050 is imperative. This goal necessitates a rapid and profound transformation of the global energy system, shifting away from fossil fuels toward renewable sources and carbon-neutral energy carriers.

The use of hydrogen as an energy carrier within the scope of the decarbonisation of the world's energy production and utilisation is seen by many as an integral part of this endeavour [3]. The primary significance of this technology is its potential to decarbonize "hard-to-abate" categories. These are areas where implementing direct electrification is either financially prohibitive or technically impractical. Prominent examples of such fields include heavy manufacturing, specifically steel and chemical production, as well as long-distance logistics like maritime freight and air travel.

Although hydrogen functions as a zero-emission fuel during consumption, its synthesis currently entails a significant carbon footprint. During 2022, the worldwide output amounted to 95 Mt, yet this supply relied predominantly on fossil fuel sources lacking carbon capture technology [4]. This dependence resulted in the generation of more than 900 Mt of CO_2, a volume roughly equivalent to the pollution produced annually by the entire aviation sector [4].

Nowadays, there are two different and mature technologies for creating green hydrogen [5]:

- **Alkaline electrolysis:** the most mature and cost-effective technology, utilizing a liquid electrolyte (KOH) and nickel-based electrodes. Nevertheless, suffers from low current densities and poor dynamic response to intermittent renewables [6].
- **Polymer Electrolyte Membrane Electrolysis (PEM Electrolysis):** offers faster response times suitable for coupling with intermittent renewables, but it faces a severe material scalability constraint due to the use on materials such as iridium and platinum [6].

Electrolysis is the primary pathway for green hydrogen, but current technologies face significant scalability hurdles regarding materials, such as the actual manufacturing prices that exceed two times the expense of conventional fossil-fuel hydrogen [6]. Therefore, the central difficulty lies in mitigating these high operational costs to improve market viability.

To overcome the limitations of critical materials and high costs, thermochemical cycles, specifically the Steam-Iron Process (SIP), that generates hydrogen by oxidizing reduced iron with steam, have gained renewed attention giving the number of distinct advantages over conventional electrolysis [7]:

- It utilizes widely available and inexpensive iron oxides, eliminating dependence on critical metals like iridium or rare earths. Moreover, unlike electrolysis, which is rigid in its need for high-purity electricity and water, SIP can be driven by low-quality gas streams such as biogas, bioethanol or syngas [7].
- SIP minimises thermodynamic losses by directly converting the chemical energy of the fuel into the chemical energy of hydrogen. Electrolysis strongly depends on the source and availability of electricity, typically generated from thermal processes, and involves significant exergy losses converting [7].
- It produces high-purity hydrogen and a separate stream of pure CO_2 without the need for complex gas separation units, allowing the capture of CO_2 for storage or other uses and making the hydrogen generation greener with negative emissions [7].

2. Background

2.1. Fluidized Bed Technology

Fluidized Bed Reactors (FBR) constitute a cornerstone technology in multiphase chemical engineering, designed to facilitate contact between solid granular materials and a fluid medium (gas or liquid). The fundamental principle of fluidization occurs when a fluid is passed upwards through a particle bed at a velocity sufficient to suspend the solids. When the drag force exerted by the upward-flowing fluid counterbalances the gravitational force acting on the particles, the bed expands and exhibits hydrodynamic behaviours characteristic of liquids, such as buoyancy and high fluidity [8].

This "fluid-like" state offers distinct advantages for thermochemical processes, specifically exceptionally high heat and mass transfer coefficients and uniform temperature gradients, which are critical for controlling highly exothermic or endothermic reactions [9]. The enhanced oxygen distribution and heat transfer provided by fluidized bed technology are the main reasons why it is considered a suitable and efficient alternative for the utilization of low-cost solid fuels.

The operational behaviour of an FBR is strictly governed by the superficial gas velocity (U) and the physical properties of the particles. While FBR evolves through different hydrodynamic stages once the minimum fluidization velocity (U_{mf}) is surpassed, a relevant change occurs at high velocities [10]. Solids are entrained out of the reactor, different from the BFB, where the bed is in the reactor in stationary conditions. This requires a recirculation loop (typically with a cyclone) to return solids to the bed. This system is called circulated fluidised beds (CFB) [8].

Standard fluidized bed reactors typically use inert granular solids, most frequently silica sand (SiO_2). However, this composition is altered in advanced combustion methodologies such as Chemical Looping Combustion (CLC) and Oxygen Carrier Aided Combustion (OCAC). In these specific applications, the inert bed mass is either partially or entirely replaced by active materials that possess oxygen-transporting capabilities.

2.2. Steam-iron process

Although hydrogen is often viewed as a future energy vector, the Steam-Iron Process (SIP) is one of the oldest technologies for its production. The method dates to the early 20th century, having been originally patented by Messerschmitt in 1910 and historically employed to generate hydrogen for airships and the food industry [11]. As the oil and gas industry expanded during the mid-20th Century, new methods of high-capacity hydrogen synthesis techniques emerged due to its lower cost and economically attractive.

Historically, the SIP was operated as a batch process, meaning that all chemical reactions took place sequentially within a single reactor vessel rather than in a continuous flow of solids. The fuel used to reduce the iron was typically coal, lignite, or syngas. Nevertheless, any substance with sufficient reducing potential, such as carbon monoxide (CO), methane (CH_4), or biomass-derived gases, can drive the reduction of the iron oxide [12].

The process consists of a cyclic redox (reduction-oxidation) mechanism involving a metal oxide, traditionally iron oxides (Fe_xO_y) being reduced to metallic iron (Fe). The initial stage of the process starts with the transformation typically progresses from hematite (Fe_2O_3) to magnetite (Fe_3O_4) and subsequently to wustite (FeO); in fluidized beds applications however, reduction to metallic iron (Fe) is typically avoided. Following this stage, the reactive atmosphere is transitioned to steam to initiate the subsequent oxidation cycle [13].

- **Step 1:** If, as an example, CO is chosen as the reduction gas, at 800–1000°C, coal or biomass facilitates the reduction of Fe_2O_3 to FeO or Fe. The reduction phases are endothermic [13].

$$\boldsymbol{3Fe_2O_3(s) + CO(g) \rightarrow 2Fe_3O_4(s) + CO_2(g)} \quad (1)$$

$$\boldsymbol{Fe_3O_4(s) + CO(g) \rightarrow 3FeO(s) + CO_2(g)} \quad (2)$$

$$\boldsymbol{FeO(s) + CO(g) \rightarrow Fe(s) + CO_2(g)} \quad (3)$$

- **Step 2:** At 600–700°C, steam is used to oxidize FeO or Fe. This phase produces a clean gas effluent that is completely free from tars or harmful pollutants.

$$\boldsymbol{Fe(s) + H_2O\ (g) \rightarrow FeO(s) + H_2(g)} \quad (4)$$

$$\boldsymbol{3FeO(s) + H_2O\ (g) \rightarrow Fe_3O_4(s) + H_2(g)} \quad (5)$$

- **Step 3:** At 850–1000°C, the oxidation of Fe_3O_4 using steam to Fe_2O_3 is not viable due to thermodynamic limitations so it must be done with air [13]. This reaction is strongly exothermic, and it ends the sequential process loop recovering heat.

$$4Fe_3O_4(s) + O_2(g) \rightarrow 6Fe_2O_3(s) \quad (6)$$

Nevertheless, the equilibrium between the different iron oxide phases is closely related to the efficiency of the SIP, reflecting the thermodynamic constraints of the process. At temperatures below approximately 570°C, FeO becomes thermodynamically unstable [14]. Therefore, to maximise process efficiency and ensure phase stability, the SIP is typically operated within the 600–900°C temperature range. Moreover, if CO is used as a reduction gas, there is a risk that the carbon could deposit on the iron, contaminating the hydrogen during the oxidation phase through the Boudouard reaction [15]:

$$2CO \rightarrow C + CO_2 \quad (7)$$

There is also another way that could happen that using methane through its decomposition:

$$CH_4 \rightarrow C + 2H_2 \quad (8)$$

With the shift towards a greener economy, nowadays SIP has regained interest among the researchers. The architecture of the steam-iron cycle permits the isolation of high-purity CO_2 into a dedicated stream, positioning this method as an effective solution for hydrogen manufacturing integrated with carbon capture. The development of chemical-looping technologies could lead to a new modern steam-iron process.

2.3. Chemical-looping technologies

2.3.1. Chemical Looping Combustion (CLC)

Chemical Looping Combustion (CLC) is an innovative technology within the field of Carbon Capture and Storage (CCS) that allows for the combustion of fuels with inherent separation of CO_2 [16]. In contrast with some traditional combustion processes, CLC avoids the direct mixing of fuel and air by using two separate reactors and a metal oxygen carrier (fully oxidized as M_xO_y), introduced in the fuel reactor to transport oxygen into the combustion zone and where it is reduced to M_xO_{y-1} according to the following reaction:

$$(2n + m)\, M_x O_y \; + \; C_n H_{2m} \rightarrow (2n + m)\, M_x O_{y-1} + nCO_2 + mH_2O \qquad (9)$$

The reduction can be sightly exothermic but is often endothermic, depending on the oxygen carrier and the fuel. For biomass-based fuels and iron-based oxygen carriers, the reduction is almost adiabatic [17]. Provided that complete fuel oxidation occurs, the flue gas exiting the fuel reactor consists solely of CO_2 and H_2O. Consequently, pure CO_2 is obtainable by lowering the temperature to condense and extract the water condensate. The oxygen carrier, still in its reduced form M_xO_{y-1}, then conveyed into the air reactor and oxidized by atmospheric oxygen, as described by the following chemical relationship:

$$M_x O_{y-1} \; + \frac{1}{2} O_2 \rightarrow M_x O_y \qquad (10)$$

This reaction is always exothermic and gives the heat necessary for the overall process [18]. The flue gas that exits the air reactor contains N_2 with some traces of unused O_2. The fully oxidised oxygen carrier (M_xO_y) is moved again to the fuel reactor where it will react again with the fuel. In the end, the highly concentrated stream of CO_2 is ready for compression and geological storage without the need for expensive external separation units.

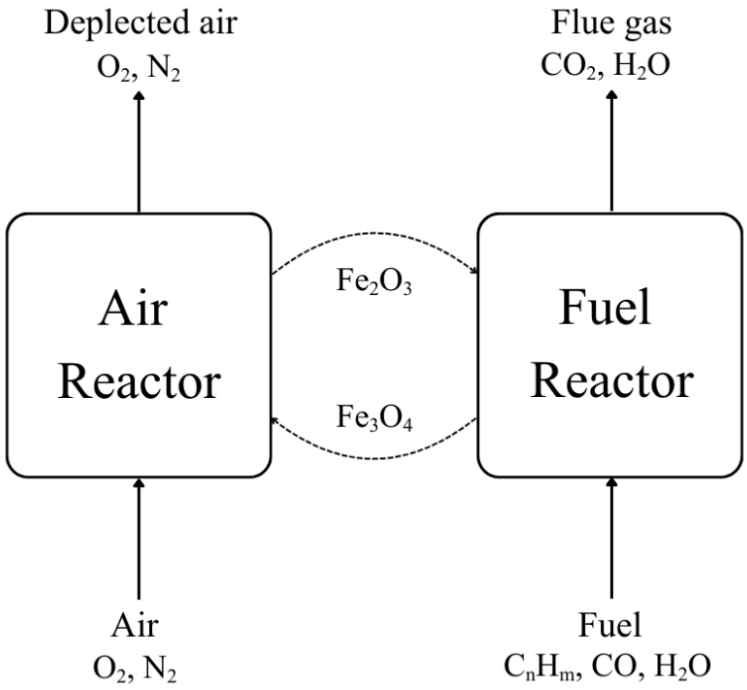

Figure 1: *Schematic description of CLC using as an oxygen carrier iron oxide.*

2.3.2. Chemical Looping Water Splitting (CLWS)

Based on the CLC reactor configuration and the chemical principles of the steam-iron reaction, CLWS represents an engineering evolution that typically employs a system of interconnected fluidized beds to allow continuous operation. This new configuration is designed to produce pure H_2 by utilising the redox properties of a solid oxygen carrier, often an iron-based compound [19].

The continuous process is carried out using three interconnected reactors: the fuel reactor (FR) and the air reactor (AR), which are also used in conventional CLC systems, along with an additional steam reactor (SR). The overall configuration is illustrated in Figure 2.

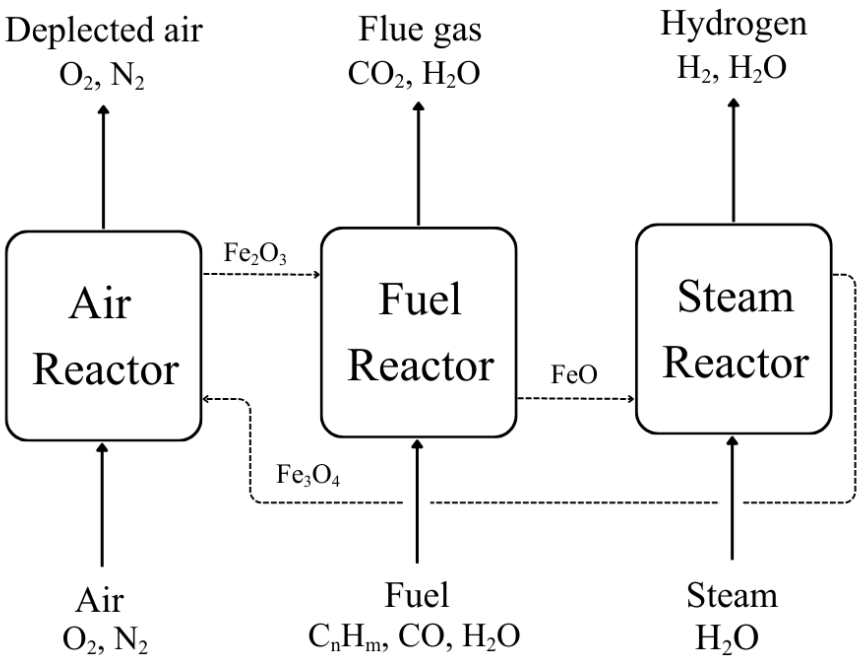

Figure 2: *A conceptual overview of the production of H_2 through the steam-iron reaction by applying chemical-looping principles.*

In the fuel reactor, the oxygen carrier (Fe_2O_3) is reduced by reacting with a hydrocarbon fuel (C_nH_m), such as syngas, methane or gasified biomass. The solid material gives up its lattice oxygen to the fuel, producing a concentrated stream of CO_2 and H_2O that is easily captured after the steam is condensed. (11) and (12), it is used Fe_2O_3 as an oxygen carrier and the reactions are unbalanced.

$$\boldsymbol{Fe_2O_3(s) + C_nH_m(g) \rightarrow Fe_3O_4(s) + CO2(g) + H_2O(g)} \quad (11)$$

$$\boldsymbol{Fe_3O_4(s) + C_nH_m(g) \rightarrow 3FeO(s) + CO2(g) + H_2O(g)} \quad (12)$$

The reduced oxygen carrier (FeO) is then transported to the steam reactor, where it reacts with H_2O. Water molecules split and extract their oxygen to partially re-oxidize itself, turning into Fe_3O_4, thereby releasing a high-purity hydrogen stream as the byproduct.

$$\mathbf{3}\boldsymbol{FeO}(\boldsymbol{s}) + \boldsymbol{H_2O}\ (\mathbf{g}) \rightarrow \boldsymbol{Fe_3O_4}(\boldsymbol{s}) + \boldsymbol{H_2}(\boldsymbol{g}) \qquad (13)$$

Finally, Fe_3O_4 is moved to the air reactor where it is fully oxidized back to its original state (Fe_2O_3) using atmospheric air to close the loop. As also happened in the CLC, the reaction with air is highly exothermic, providing the necessary thermal energy to sustain the other endothermic parts of the cycle.

$$\mathbf{4}\boldsymbol{Fe_3O_4}(\boldsymbol{s}) + \boldsymbol{O_2}(\boldsymbol{g}) \rightarrow \mathbf{6}\boldsymbol{Fe_2O_3}(\boldsymbol{s}) \qquad (14)$$

The efficiency of this system is strongly linked to the properties of the solid oxygen carrier, which must satisfy fundamental requirements such as high redox performance, rapid rates of oxygen absorption and release, structural and thermal resilience and resistance to particle attrition and thermal sintering throughout successive operational cycles. One of the main objectives involves ensuring that these functional attributes remain stable, over extended periods of operation, particularly when the system is exposed to the extreme temperatures necessary for the process [20].

For the last twenty years, scientists have been on a mission to find the perfect oxygen carrier. They have evaluated over 900 different materials through their paces, mostly focusing on transition metals such as Fe, Mn, Cu, and Ni. While those metals have been the standard, perovskite oxides are now emerging as the real favourites [20].

2.4. Perovskite oxides as oxygen carriers

Perovskites represent a category of compounds characterized by a specific crystalline arrangement, involving organic, halide, and oxide varieties. While organic and halide forms are widely utilized in photovoltaic technology, the present work concentrates specifically on the oxide subclass. Initially, the term identified the mineral $CaTiO_3$, the first to be discovered by the mineralogist Gustavus Rose in the Ural Mountains (Russia, 1834) [21].

It has since been expanded to describe a diverse family of complex metal oxides with the general formula $ABO_{3-\delta}$ where A and B are positively charged cations of different

ionic radii, with A typically being the larger ion compared to B, and O corresponds to the oxygen, a negative charge ion [21].

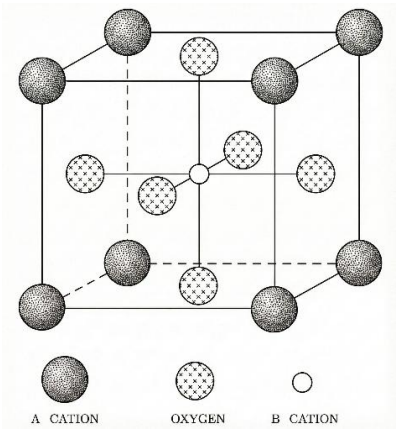

Figure 3: *The cubic perovskite structure $ABO_{3-\delta}$*

To predict whether a specific combination of elements will successfully form a stable perovskite lattice, researchers utilize the Goldschmidt tolerance factor (t). This geometric ratio is calculated using the ionic radii of the A-site cation (R_A), the B-site cation (R_B), and the oxygen anion (R_O):

$$\boldsymbol{t = \frac{R_A + R_O}{\sqrt{2}\,(R_B + R_O)}} \tag{15}$$

Generally, a stable perovskite structure is formed when t falls within the range of 0.8 to 1.0 [22]. From 0.9 to 1.0, it corresponds to a cubic structure. When $0.71 < t < 0.9$, the structure typically distorts into orthorhombic or rhombohedral symmetries. If it is significantly lower than 0.71, a trigonal and other different structures can be found, whereas values above 1.0 often lead to hexagonal, tetragonal structures or unstable lattices [23].

Furthermore, the stoichiometry can be finely tuned through partial ionic replacement at either the A or B positions with secondary elements (A' or B'). This substitution process results in the formation of solid solutions typically represented by the general formulas $A_{1-x}A'_xBO_{3-\delta}$ or $AB_xB'_{1-x}O_{3-\delta}$.

The variable δ (delta) represents the oxygen non-stoichiometry factor, which quantifies the concentration of oxygen vacancies within the crystal lattice.

Unlike simple metal oxides where oxygen loss often triggers a phase change, for instance from hematite Fe_2O_3 to magnetite Fe_3O_4, perovskites can accommodate a

significant variation in oxygen content while maintaining their primary crystallographic structure [24].

When the material is exposed to a reducing environment, oxygen ions (O^{2-}) leave the lattice to react with the fuel, leaving behind vacancies and increasing the value of δ. Contrariwise, during oxidation (high oxygen partial pressure or steam), oxygen from the gas phase fills these vacancies, decreasing δ back towards zero.

The magnitude of δ is a direct indicator of the Oxygen Exchange Capacity (OEC) of the material. A higher capacity to vary δ without decomposing means the material can transport more oxygen per cycle, which directly correlates to a higher yield of hydrogen production in the subsequent steam step. The value of δ is not constant, it is a function of temperature (T) and oxygen partial pressure (pO_2).

This configuration allows the crystalline structure to be extremely flexible, enabling the partial substitution of its components to "tune" its chemical properties according to the specific needs of the process. By substituting elements at the A or B sites, one can engineer the bond strengths within the lattice to favour the formation of vacancies at specific operating conditions, thereby optimizing the kinetics of water splitting.

3. Aim of the project

Based on the context established in the previous section regarding the limitations of current electrolysis technologies and the potential of the Steam-Iron Process, this thesis focuses on the development of advanced Oxygen Carriers (OC). While iron oxides are abundant, their performance can be limited by sintering and slow reaction kinetics. Therefore, this project explores the use of perovskite-type oxides ($ABO_{3-\delta}$) as a tuneable alternative to enhance the efficiency of hydrogen production.

The primary aims of this thesis are:

- To establish a reliable synthesis methodology for specific perovskite formulations.
- To verify the formation of the perovskite phase and evaluate the structural integrity of the synthesized materials using XRD.
- Evaluate the redox activity and oxygen exchange capacity of the candidates under simulated cyclic conditions using TGA.

This project identifies perovskite-type oxides as a superior alternative. These materials offer immense chemical flexibility, allowing for the substitution of cations at the A and B sites. This flexibility enables the precise engineering of their redox properties, oxygen mobility, and thermal stability to meet the rigorous requirements of fluidized bed operations.

3.1. Objectives and limitations

To achieve the primary aim, this thesis is structured around four specific activities. The first phase involves the development of a synthesis methodology to establish a robust and reproducible protocol capable of producing high-quality perovskite powders. Once the method is defined, the project will proceed to material selection and synthesis, where a series of candidate materials will be chosen based on thermodynamic criteria and a comprehensive literature review to synthesize a defined set of samples.

Following the synthesis step, the materials will be subjected to comprehensive physicochemical characterisation to verify that the perovskite structure has been correctly generated and to guarantee high crystallographic purity by detecting any impurities or secondary phases.

Finally, and subject to time constraints, an initial performance assessment will be conducted to investigate the redox activity and hydrogen production capacity of the synthesized materials under simulated Steam-Iron Process conditions.

In line with the objectives outlined above, this thesis seeks to answer the following key research questions:

- Is the proposed synthesis methodology effective in yielding phase-pure perovskite structures for the selected compositions?
- How does the oxygen deficiency (δ) of the synthesized perovskites change as a function of temperature?
- Do the synthesized perovskites demonstrate the necessary redox properties to serve as viable candidates for hydrogen production in the Steam-Iron Process?

The primary limitations of this project arise from time constraints and the vast number of possible perovskite compositions. The range of elements tested at the A- and B-sites of the perovskite structure will be limited. These compounds were selected based on their thermodynamic and chemical properties. Also, the study will not discuss where raw materials come from or how to acquire them.

Another factor to be considered concerns the redox testing stage. Depending on the available time and the outcomes of the perovskite synthesis, not all samples will be subjected to redox testing. The selection of samples will be based on the purity of the perovskite structure, as determined from the prior structural characterization analyses.

4. Method

The experimental work involved preparing 22 samples of perovskite structure. Some samples will have a different formula that can be expressed as $ABB'O_{3-\delta}$, where B and B' represent two distinct cations from different elements, as well as $AA'BO_{3-\delta}$ which also corresponds to two different cations.

4.1. Preparation

After analysing a wide range of elements that could be suitable for achieving a perovskite crystal structure, the following combinations have been selected for the preparation of the samples.

Table 1: *List of sample numbers and chemical formulas with the A-site and B-site substitution ratios.*

		A	**A'**	**B**	**B'**	**Goldsmidt factor (t)**
	Name	**Ca** [x]	**La** [1-x]	**Fe** [x]	**Mn** [1-x]	
Sample 1	$CaMnO_{3-\delta}$	1	0	0	1	0.947
Sample 2	$CaFeO_{3-\delta}$	1	0	1	0	0.947
Sample 3	$LaMnO_{3-\delta}$	0	1	0	1	0.954
Sample 4	$LaFeO_{3-\delta}$	0	1	1	0	0.954
Sample 5	$CaFe_{0.2}Mn_{0.8}O_{3-\delta}$	1	0	0.2	0.8	0.947
Sample 6	$CaFe_{0.8}Mn_{0.2}O_{3-\delta}$	1	0	0.8	0.2	0.947
Sample 7	$CaFe_{0.5}Mn_{0.5}O_{3-\delta}$	1	0	0.5	0.5	0.947
Sample 8	$LaFe_{0.2}Mn_{0.8}O_{3-\delta}$	0	1	0.2	0.8	0.954
Sample 9	$LaFe_{0.8}Mn_{0.2}O_{3-\delta}$	0	1	0.8	0.2	0.954
Sample 10	$LaFe_{0.5}Mn_{0.5}O_{3-\delta}$	0	1	0.5	0.5	0.954
Sample 11	$Ca_{0.2}La_{0.8}FeO_{3-\delta}$	0.2	0.8	1	0	0.953
Sample 12	$Ca_{0.8}La_{0.2}FeO_{3-\delta}$	0.8	0.2	1	0	0.949
Sample 13	$Ca_{0.5}La_{0.5}FeO_{3-\delta}$	0.5	0.5	1	0	0.951

For the samples containing a mixture of Ca and La at the A-site, Fe was selected for the B-site due to its higher oxygen exchange capacity and superior reactivity with oxygen than Mn.

Table 1 also reports the Goldschmidt tolerance factor of each sample, calculated with (15). The calculated tolerance factor (t) values are very close to 1, reflecting the similar ionic radii of the A-site cations and indicating a strong tendency toward the formation of an ideal perovskite structure. The ionic radii used in these calculations that depends on the composition and assuming $\delta=0$, are presented in Table 2.

Table 2: *Ionic radii of constituent A-site and B-site cations and the oxygen anion*

	Ionic radii (Å)
R_A (Ca^{2+})	1.34
R_A (La^{3+})	1.36
R_B (Fe^{3+})	0.645
R_B (Mn^{4+})	0.53
R_B (Mn^{3+})	0.645
R_O (O^{2-})	1.40

4.2. Synthesis

The experimental work was divided into two parts. The first part focused on the synthesis of Sample 1, corresponding to calcium manganate ($CaMnO_{3-\delta}$), for which ten individual samples (S1.1–S1.10) will be prepared. The second part will involve the synthesis of the remaining samples (S2–S13), following the same methodology as in S1, which will serve as a reference for the subsequent experiments.

4.2.1. Preparation of PVA-solution

For the synthesis of the first sample, we will use PVA (polyvinylalcohol) that will help keep the ions uniformly mixed in solution. To produce a PVA, polyvinylalcohol, (10 %) solution with water, the following steps will be followed:

1. Heating the water ($m_W = 500\ mL$)
2. Add the PVA crystals ($m_{PVA} = 50g$) until they are fully solved into the water (requires constant heat and stirring)
3. Water should evaporate at a fast pace, during heating up, cooling down and of course in between.
4. During the cooldown phase, the PVA solution thickens and becomes ready for its use.

4.2.2. Preparation of the samples

The second step involves calculating the quantities needed to obtain the desired stoichiometry, along with defining the composition of the final mixture. Starting with Sample 1 ($CaMnO_{3-\delta}$) for instance, the synthesis will be designed to produce approximately 5 g of calcium manganate as the final product with a fixed 2 g CaO. The

final solution volume was intentionally kept small, as these first ten samples are meant to be produced under test conditions.

According to (23), each mole of CaO produces one mole of $CaMnO_3$, while one mole of Mn_2O_3 is equivalent to two moles of CaO. This stoichiometric ratio makes it possible to determine the necessary amounts of the precursors. By combining this relationship with the molar masses of the compounds involved, the required quantity of Mn_2O_3 can be calculated using (36). Using this formula, approximately 2.82 g of Mn_2O_3 is required, considering the conditions described above.

The same process will be used for the other samples (S2-S13). The necessary quantities of the A- and B-site precursor compounds for the rest of the samples were determined based on their stoichiometric proportions and the chemical reactions that will take place in each of the prepared samples (24)-(35). Table 10 summarizes the formulas and atomic weights used to determine the masses of the initial precursor compounds employed in the synthesis of all the samples.

Table 3 shows the results obtained for each compound using the formulas described above.

Table 3: *Masses of the precursor compounds from sample 1 to 13*

Sample	CaO [g]	La_2O_3 [g]	Fe_2O_3 [g]	Mn_2O_3 [g]
1	2	—	—	2.8
2	2	—	2.8	—
3	—	3.4	—	1.6
4	—	3.4	1.6	—
5	2	—	0.6	2.3
6	2	—	2.2	0.5
7	2	—	1.4	1.4
8	—	3.4	0.3	1.3
9	—	3.4	1.3	0.3
10	—	3.4	0.8	0.8
11	0.3	2.9	1.8	—
12	1.4	1	2.4	—
13	0.7	2.1	2.1	—

4.2.3. Sintering

The first step consisted of mixing and combining the ingredients with the aim of forming granules. For Sample 1.1 to 1.10, the mixture was prepared using manganese

oxide and calcium oxide as the primary precursors, together with a binder solution composed of 10 wt% polyvinyl alcohol (PVA). There are different procedures in order to mix all the compounds properly, the batch added material (BaM) is the one used for this experiment, whose function is to add all the components in one batch while mixing. The PVA solution was sprayed onto the mixture using a spray bottle, ensuring it to be distributed in the form of very small droplets. Once the mixture became homogeneous, the amount of binder added was recorded, and the mixture was evenly distributed into the first five crucibles (Samples 1.1 to 1.5), see Figure 4. For the remaining five crucibles, an additional drop of PVA binder was added to the mixture before distributing it among them.

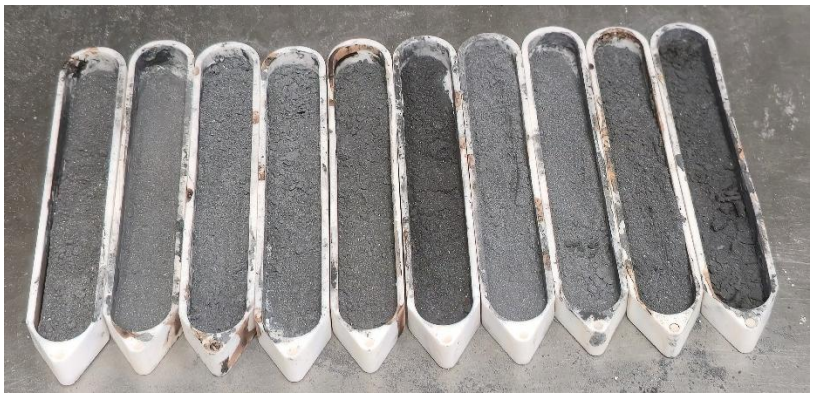

Figure 4: *The samples 1.1 to 1.10, from left to right, containing the mixture after the addition of the PVA binder.*

Although the samples display different shades of grey, they all originate from the same batch. The darker tones of samples 1.6 and 1.10 are likely due to the samples that were positioned at the bottom of the mixture during processing.

For the remaining samples (S2–S10), the preparation procedure was identical to that applied to Samples 1.5–1.10, including the use of the same PVA content (two more drops than 1.1-1.5) to ensure consistent granulation conditions.

Figure 5: *The samples 2 to 13, from left to right, containing the mixture after the addition of the PVA binder.*

All samples were subjected to high-temperature treatment to promote the formation of the perovskite phase. The furnace was programmed to reach 300 °C in approximately 1 h and hold this temperature for an additional hour. This stage is needed for the controlled decomposition of the PVA binder that was used previously in the granulation process. Subsequently, the temperature was increased to 800 °C at a heating rate of 5 °C min^{-1} and maintained for 2 h. The system was then further heated to 1250 °C at the same rate, where the samples were sintered for 9 h to achieve sufficient densification of the granules. Finally, the temperature was gradually reduced to room temperature.

4.3. X-ray Diffraction Analysis

The next step will be to analyse these particles to determine their composition and structure. The characterization of the oxygen carriers was performed using X-ray Diffraction (XRD), a powerful non-destructive technique for analysing solid materials. The objective was to verify the presence of perovskite phase within the synthesized samples.

The specific atomic arrangement within the unit cells of perovskite lattices causes incident X-ray beams to scatter across a variety of distinct vector paths. A detector records both the angle and strength of this scattered light, producing a signal that plots intensity against the diffraction angle. This resulting graph, known as a diffractogram, allows researchers to determine the precise atomic layout and structural properties of the crystal [25].

The core principle of X-ray diffraction relies on the ability of electromagnetic radiation in the nanometer range to interact with atomic electrons. This interaction creates interference patterns whenever the distance between atoms in a specimen matches the X-ray wavelength.

Constructive interference takes place provided that the scattered waves remain in phase. Under these conditions, the combined wave amplitudes increase, although the wavelength remains unchanged [26]. On the other hand, when waves are out of phase, the result is destructive or partially destructive interference, leading to a reduction in the final signal strength. In cases where the destructive effect is complete, the resulting wave amplitude drops to zero.

In the XRD patterns, a diffraction peak is simply the exact point where the waves combined in phase. The observation of a high-intensity peak indicates that a significant number of ordered atomic planes are contributing to this constructive interference. In opposition, the baseline regions of the diffractogram represent zones where destructive interference dominates, resulting in flat area of the graph.

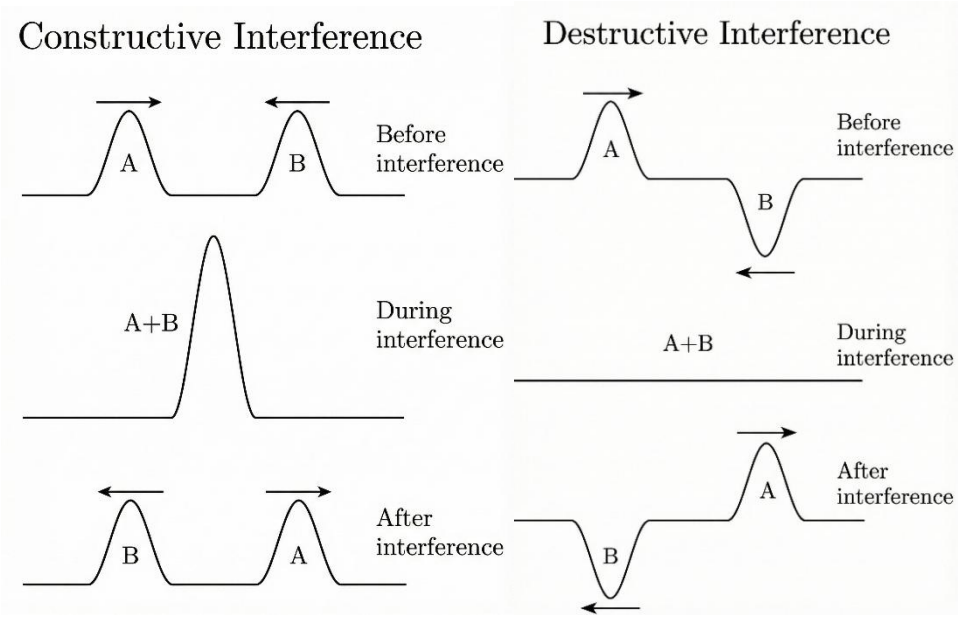

Figure 6: *Mechanisms of constructive and destructive wave interference*

The phenomenon of wave interference within crystalline structures is governed by Bragg's Law. This principle dictates the conditions under which constructive interference occurs, allowing for the determination of internal lattice dimensions. The equation of Bragg's law is the following one:

$$\boldsymbol{n \cdot \lambda = 2 \cdot d \cdot \sin(\theta)} \qquad (16)$$

In (16, n is a positive integer representing the reflection order (1, 2, 3,…), λ signifies the wavelength of the incoming X-ray radiation, d is the interplanar distance between

successive layers of the crystal lattice and θ is the angle of incidence relative to the lattice planes.

Conventional XRD systems utilize an X-ray tube as a source to direct a focused beam toward the specimen at a specific angle (θ). As this angle is incrementally adjusted during the scan, a detector captures the resulting spectrum of scattered radiation. The detection process involves the use of a transducer to quantify the photons from the scattered radiation. This data is used to generate a unique diffraction profile, which serves as a structural "fingerprint" for the specimen.

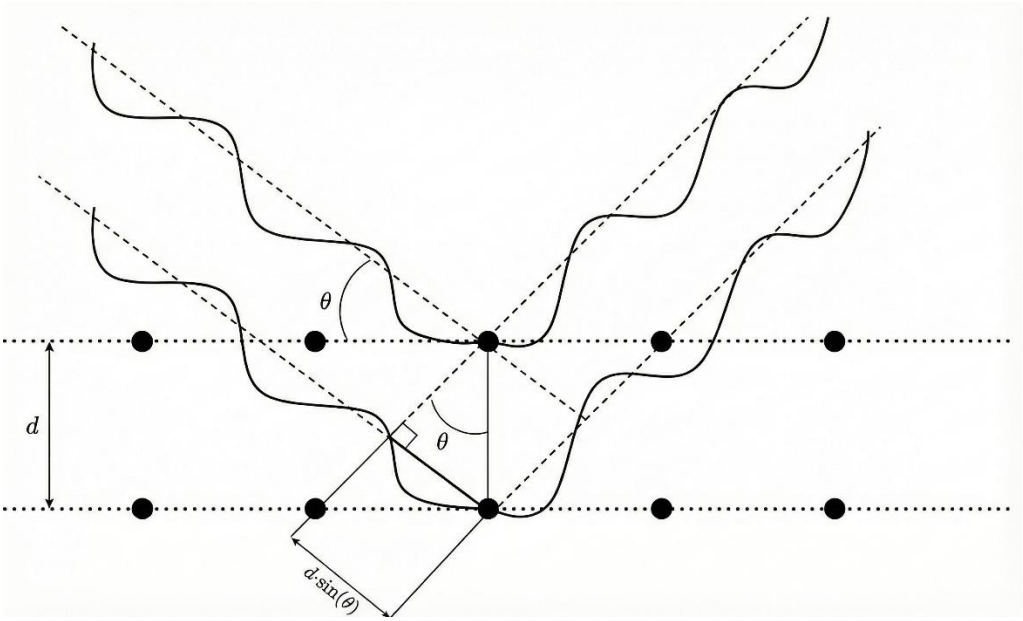

Figure 7: *Illustration of X-ray diffraction occurring between two crystallographic planes.*

The X-ray Diffraction (XRD) analysis was carried out using a BRUKER D8 Discover all-purpose X-ray diffractometer equipped with Cu radiation (λ = 1.54 Å). The data obtained was visualized and analysed using DIFFRAC.TOPAS and DIFFRAC.EVA softwares. The data was taken with the step-by-step scanning ($\Delta 2\theta = 0.03°/s$) operating at 40 kV and 40 mA, from 10° to 90°. The XRD pattern was conducted under regulated thermal and atmospheric conditions. The acquisition of data took a period of 40 minutes for each individual sample scan.

Initially, an intensity versus diffraction angle (2θ) graph was generated, allowing the software to compare the experimental pattern with reference data from the Crystallography Open Database (COD) and PDF-4+ 2025 database, which contains diffraction patterns for a wide range of crystalline materials and powders. Then, the software calculated a Figure of Merit (FOM) for each possible match, ranking them according to their degree of correspondence with the experimental data. The 4 highest-

ranking matches were subsequently examined visually to verify which diffraction peaks of the sample corresponded to those of the reference patterns.

4.3.1. Diffractogram analysis

Based on the results of the diffractograms, the objective was to see which percentage of perovskite structure had form in the analysed sample.

To achieve this, the semiquantitative percentages provided by the software were examined to obtain an approximate estimation of the phases present in each sample, based on the elements detected in the diffractogram. It is important to note that these values do not represent the exact amount of perovskite structure formed during the high-temperature synthesis. The perovskite content was calculated by summing the percentages of all identified crystalline phases that exhibit a perovskite structure, while impurity phases were excluded from this calculation.

4.4. Thermogravimetric Analysis (TGA)

The oxygen carrying capacity of the synthesized perovskites was evaluated using Thermogravimetric Analysis (TGA). This technique quantifies the mass variation of a sample as a function of temperature and time under a controlled gaseous atmosphere. Specifically, TGA allows for the precise determination of reaction kinetics by correlating mass gain and loss with the oxidation (oxygen uptake) and reduction (oxygen release) of the perovskite lattice, respectively.

The apparatus used for this analysis is known as a thermogravimetric analyser (TGA Q500). The system comprises three critical components:

- **The Thermobalance:** an electronic microbalance capable of measuring mass changes with high precision, typically in the range of microgram (μg) sensitivity. The sample is placed in a crucible, typically constructed of aluminium, which is mechanically connected to the weighing mechanism.
- **Furnace**: surrounds the sample holder and is controlled by a temperature programmer. It can operate from ambient temperatures up to 1000ºC or 1600ºC.
- **Atmosphere gas:** A controlled gas flows through the furnace to establish the experimental environment. There will be 3 types of gases in this case:
    - **Inert Gas:** Used to investigate thermal decomposition.
    - **Oxidation gas:** Used to investigate oxidative degradation processes.
    - **Reduction gas**: Used to investigate reductive processes.

The experimental design aimed to replicate the Chemical Looping Water Splitting (CLWS) technique. Despite the fact that steam (H_2O) is the chosen oxidizing agent for this utility, technical obstacles concerning steam injection averted its usage on the tests [27]. As a result, a CO/CO_2 redox pair were selected as the reducing and oxidizing dealers, respectively, because of their similar thermodynamic traits and redox activity in relation to the H_2/H_2O pair [28].

CO acts as a reducing agent, removing lattice oxygen to generate vacancies (δ) and reduce B-site oxidation states. Conversely, CO_2 acts as an oxidant for the oxygen-deficient perovskite, which thermodynamically drives CO_2 dissociation to refill the crystal lattice.

$$\boldsymbol{ABO_3 + \delta CO \rightleftharpoons ABO_{3-\delta} + \delta CO_2} \tag{17}$$

$$\boldsymbol{\Delta\delta = \frac{m_0 - m_f}{m_0} \cdot \frac{M_{ABO_3}}{M_O}} \tag{18}$$

$$\boldsymbol{t_{red}[s] = 60 \cdot \frac{\frac{m_{ABO_3}}{1000 \cdot M_{ABO_3}} \cdot \delta}{\frac{\dot{V}_{CO}}{V_{m,CO}}}} \tag{19}$$

$$\boldsymbol{t_{ox}[s] = 60 \cdot \frac{\frac{m_{ABO_3}}{1000 \cdot M_{ABO_3}} \cdot \delta}{\frac{\dot{V}_{CO_2}}{V_{m,CO_2}}}} \tag{20}$$

The theoretical duration required for the reduction and oxidation half-cycles was calculated using (19)-(20), where m_{ABO3} and M_{ABO3} is the mass and molar mass of the sample to analyse in the TGA, respectively, $\dot{V}_{CO/CO_2}$ is the flux rate of CO/CO_2 and $V_{m,CO/CO_2}$ is the molar volume of CO/CO_2. This calculation imposes a stability constraint on the oxygen non-stoichiometry parameter (δ), limiting it to a maximum value of 0.5. This threshold was established to prevent the decomposition of the perovskite lattice during the process.

To calculate Δδ, (18) is used where m_0 and m_f is the initial and final mass respectively, and M_O is the atomic mass of oxygen.

$$\boldsymbol{\%_{loss} = \left(\frac{\delta \cdot M_O}{M_{ABO_3}}\right) \cdot 100} \tag{21}$$

$$\boldsymbol{Mass\ lost\ [mg] = \frac{m_{ABO_3} \cdot \%_{loss}}{M_{ABO_3}}} \tag{22}$$

(21) and (22) were used to calculate the percentage of mass loss and the exacts mass lost of the perovskite present in the samples assuming the maximum mass corresponds to $\delta = 0$.

Theoretical calculations predicted extremely rapid reduction and oxidation times, ranging between 0.5 and 3 seconds depending on sample mass and gas flow rates. Despite these calculations, the theoretically estimated reduction and oxidation times were considered unreliable, as such processes typically take significantly longer in practice. Consequently, the optimal experimental parameters for the TGA were established empirically through iterative experimental testing.

In a standard procedure, a sample mass of approximately 10–20 mg is loaded into the crucible. The system is tared to establish the initial mass (m_0). The TGA profile consisted of a heating rate of 25 °C/min up to 900°C, 800°C and 700°C, followed by a 200-minute isothermal dwell, in different runs. This isothermal period covered the duration of two redox cycles, during which instantaneous mass (m), temperature (T), and time (t) were recorded. The program concluded by cooling the system to ambient conditions.

During a single cycle, the atmospheric composition was modulated by switching between three selected gases. These gases were introduced into the reaction chamber in the following order:

Table 4: *Operating conditions for reduction-oxidation cycle*

Step	Operation	Rate [°C/min]	Target Temp [°C]	Gas Components	Concentration [vol%]	Flow Rate [mL/min]
1	Heating	25	900/800/700	Air	21% O_2 / 79% N_2	90
2	Stabilization	Isotherm	900/800/700	Air	21% O_2 / 79% N_2	90
3	Flush 1	Isotherm	900/800/700	N_2	100% N_2	90
4	CO Reduction	Isotherm	900/800/700	CO	100% CO	90
5	Flush 2	Isotherm	900/800/700	N_2	100% N_2	90
6	CO_2 Oxidation	Isotherm	900/800/700	CO_2	100% CO_2	90
7	Flush 3	Isotherm	900/800/700	N_2	100% N_2	90

8	Regeneration	Isotherm	900/800/700	Air	21% O_2 / 79% N_2	90
9	Cooling	50	25	Air	21% O_2 / 79% N_2	90

After performing several tests at the three selected temperatures over multiple redox cycles, the temperature that provides the best overall performance during both reduction and oxidation will be selected. This selection will be based on the operating condition that ensures greater sample stability throughout the process, combined with slower reduction kinetics and faster oxidation kinetics, as normally by decreasing the temperature reduces the reaction rate during the reduction step while enhancing the reaction rate during oxidation. Based on the observations made during the tests, the durations for the reduction and oxidation steps were set to 1 minute and 90 minutes, respectively.

The selection of the best-performing perovskites during the redox cycle will be based on the evolution of their oxygen non-stoichiometry (δ). The perovskite exhibiting the highest oxygen exchange capacity (OEC) per cycle, i.e., the highest δ, will be selected, provided that it does not exceed the limit of 0.5 at any point. Samples exceeding this threshold will be considered unsuitable for the process. It also will be suitable for that the thermal stability during the heating up to the operating temperature.

5. Results and discussion

5.1. Results from the synthesis and sieving

After sintering, the samples developed a darker tone, as shown in Figure 8. Upon visual inspection, noticeable differences in grain size can be observed among the samples.

Figure 8: *Samples 1.1 to 1.10 corresponding to* $CaMnO_{3-\delta}$

Figure 9: *Samples 2 to 13 after their removal from the high-temperature furnace*

5.1.1. Sieving process and particle classification

The next step consisted in sieve the sintered particles from each sample to obtain grains with sizes between 90 and 180 μm, which was considered the optimal range for use in fluidised bed reactors. In steam-iron process, this size enhances steam penetration and accelerates the hydrogen production rate. In general, the smaller the particle, the larger its specific surface area. However, particles smaller than 90μm are so light that the gas flow can carry them out of the reactor, causing them to escape through the upper section and less suitable for continuous operation, as a significant amount of material would be rapidly lost.

For this purpose, a sieve shaker is used. It contained a stack of sieves with different mesh sizes and mechanically shacked them, allowing smaller particles to pass through while retaining larger ones. In this setup, two sieves were employed: the lower sieve filters out particles smaller than 90 μm, while the upper sieve retains those smaller than 180 μm.

The samples were sieved, the resulting granules were weighed, and the data obtained are summarized in the following table.

Table 5: *Weight of granules for different size ranges*

Sample	Weight before sieving [g]	Weight granules (90-180 μm) [g]	Weight granules (<90 μm) [g]	Losses during sieving [g]	Percentage of granules (90-180 μm) [%]
1.1 - $CaMnO_{3-\delta}$	4.3	1	3.3	0	23.25
1.2 - $CaMnO_{3-\delta}$	3.9	1.6	2.1	-0.2	41.02
1.3 - $CaMnO_{3-\delta}$	4.4	1.1	2.8	-0.5	25
1.4 - $CaMnO_{3-\delta}$	4.6	2	2.5	-0.1	43.47
1.5 - $CaMnO_{3-\delta}$	4.6	2.1	2.5	0	45.65
1.6 - $CaMnO_{3-\delta}$	3.8	2.1	1.5	-0.2	55.26
1.7 - $CaMnO_{3-\delta}$	6.3	2.2	3.8	-0.3	35
1.8 - $CaMnO_{3-\delta}$	4.1	1.3	2.2	-0.6	31.70
1.9 - $CaMnO_{3-\delta}$	4.3	1.5	2.4	-0.4	34.88
1.10 - $CaMnO_{3-\delta}$	4.4	3.1	1.3	0	70.45
2 - $CaFeO_{3-\delta}$	3.1	1.4	1.5	-0.2	45.16
3 - $LaMnO_{3-\delta}$	4.5	1.5	2.4	-0.6	33.33
4 - $LaFeO_{3-\delta}$	4.1	1.6	2.5	0	39.02

5 - $CaFe_{0.2}Mn_{0.8}O_{3-\delta}$	4.2	3.7	0.5	0	88.10
6 - $CaFe_{0.8}Mn_{0.2}O_{3-\delta}$	4.0	2.4	1.6	0	60.0.0
7 - $CaFe_{0.5}Mn_{0.5}O_{3-\delta}$	4.5	2.7	1.7	-0.1	60.00
8 - $LaFe_{0.2}Mn_{0.8}O_{3-\delta}$	4.6	1.4	3.2	0	30.43
9 - $LaFe_{0.8}Mn_{0.2}O_{3-\delta}$	4.0	1.3	2.7	0	32.50
10 - $LaFe_{0.5}Mn_{0.5}O_{3-\delta}$	3.9	1.4	2.2	-0.3	35.90
11 - $Ca_{0.2}La_{0.8}FeO_{3-\delta}$	4.8	1.5	3	-0.3	31.25
12 - $Ca_{0.8}La_{0.2}FeO_{3-\delta}$	4.5	1.5	3	0	33.33
13 - $Ca_{0.5}La_{0.5}FeO_{3-\delta}$	4.0	1.1	2.8	-0.1	27.50

The granules within the 90–180 μm size range had an average mass of 1.8 g, which corresponds to approximately 42% of the total mass of the sieved mixture.

A notable observation is that samples 1.6 to 1.10 developed a larger fraction of granules within the 90–180 μm size range compared to samples 1.1 to 1.5. This improvement occurred after adding a few additional drops of PVA, suggesting that the increased binder content enhanced granule formation in the desired size interval.

5.2. X-ray Diffraction (XRD) results

XRD was employed to identify and quantify the crystalline phases present in the synthesized samples. This technique provides detailed information on phase composition and structural arrangement, enabling the assessment of whether the targeted perovskite structures were successfully formed and to what extent secondary phases or impurities are present. The following analyses are grouped into families so as to study the evolution of both the A-site and the B-site as their composition varies.

5.2.1. Results for $CaFe_xMn_{1-x}O_{3-\delta}$

The structural analysis of the various calcium-iron-manganese oxide samples reveals distinct differences and stabilisation across the pattern.

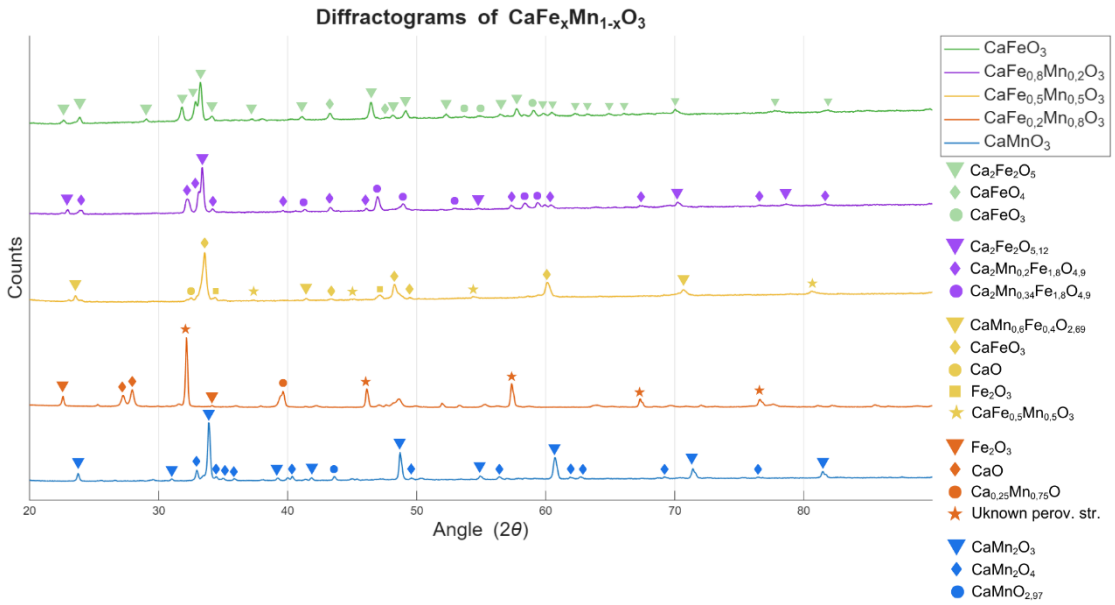

Figure 10: *Evolution of X-ray diffraction patterns for $CaFe_xMn_{1-x}O_{3-\delta}$ as a function of the iron composition (x = 1.0, 0.8, 0.5, 0.2, 0) forming $CaFeO_3$, $CaFe_{0.8}Mn_{0.2}O_3$, $CaFe_{0.5}Mn_{0.5}O_3$, $CaFe_{0.2}Mn_{0.8}O_3$ and $CaMnO_3$ going from top to bottom.*

Regarding $CaFeO_{3-\delta}$ sample, the data indicates that the stabilization of the pure phase is incomplete, so $CaFeO_3$ is not present in the XRD pattern. Several calcium-iron oxides, specifically srebrodolskite structures such as $Ca_2Fe_2O_5$ and $CaFeO_4$ were found. The identification of $Ca_2Fe_2O_5$ is particularly relevant, as a brownmillerite structure, it represents an oxygen-deficient derivative of the ideal perovskite lattice. This suggests that the sample can be structurally interpreted as containing the decomposed phase of perovskite, specifically $CaFeO_{2.5}$.

For the $CaFe_{0.8}Mn_{0.2}O_{3-\delta}$ composition, the synthesis appears less successful in achieving the target structure. Although there are high percentage matches (86-95%) with oxide phases such as $Ca_2Fe_{0.34}Mn_{1.66}O_3$ these correspond to the srebrodolskite family rather than the intended perovskite phase.

In contrast, $CaFe_{0.5}Mn_{0.5}O_{3-\delta}$ shows strong matches to $CaFeO_{3-\delta}$ (up to 90%) alongside minor $CaFe_xMn_{1-x}O_3$ mixed phases. The pattern is relatively clean and close to the theoretical $CaFe_{0.5}Mn_{0.5}O_3$ composition. This suggests successful formation of a perovskite-like phase with Mn partially substituting Fe. Some secondary phases remain, but the overall structure aligns well with the intended perovskite.

In the $CaFe_{0.2}Mn_{0.8}O_{3-\delta}$ analysis, the expected perovskite $CaFe_{0.2}Mn_{0.8}O_3$ does not appear. Instead, segregated Fe and Ca with Mn oxides dominated the diffractogram. The diffractogram peaks corresponds to a perovskite phase but due to structural

distortions, the correct entry is not recognized. By overlapping the diffractograms of Sample 9 – $LaFe_{0.8}Mn_{0.2}O_{3-\delta}$ and Sample 5 – $CaFe_{0.2}Mn_{0.8}O_{3-\delta}$, clear similarities in their diffraction patterns can be observed. Since the main peaks align, we can conclude that Sample 5 contains a perovskite fraction.

Finally, the sample $CaMnO_{3-\delta}$ shows excellent structural fidelity. The experimental peaks align closely with reference standards from the COD and PDF databases, particularly around the main diffraction angles (notably near $2\theta \approx 33°$, 47°, and 58°). This strong correspondence confirms that the intended $CaMnO_{3-\delta}$ perovskite structure is the dominant crystalline phase, with only minor deviations suggesting the presence of weak secondary manganese oxide phases.

In Figure 11, the percentage of perovskite structure identified in each analysis is presented.

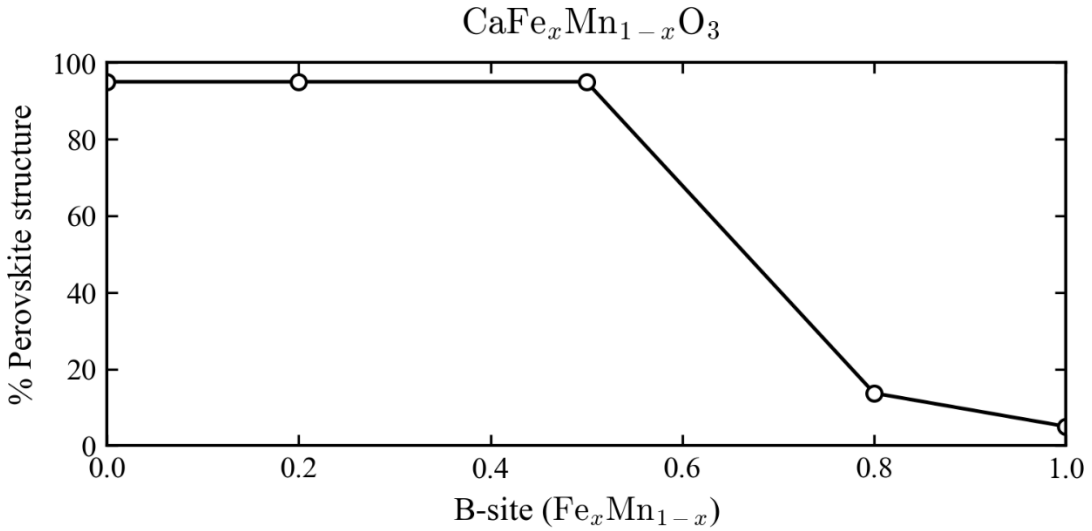

Figure 11: *Effect of B-site iron composition (x = 0, 0.2, 0.5, 0.8, 1.0) on the perovskite structure of $CaFe_xMn_{1-x}O_3$ forming $CaMnO_3$, $CaFe_{0.2}Mn_{0.8}O_3$, $CaFe_{0.5}Mn_{0.5}O_3$, $CaFe_{0.8}Mn_{0.2}O_3$ and $CaFeO_3$ going from left to right.*

5.2.2. Results in $LaFe_xMn_{1-x}O_{3-\delta}$

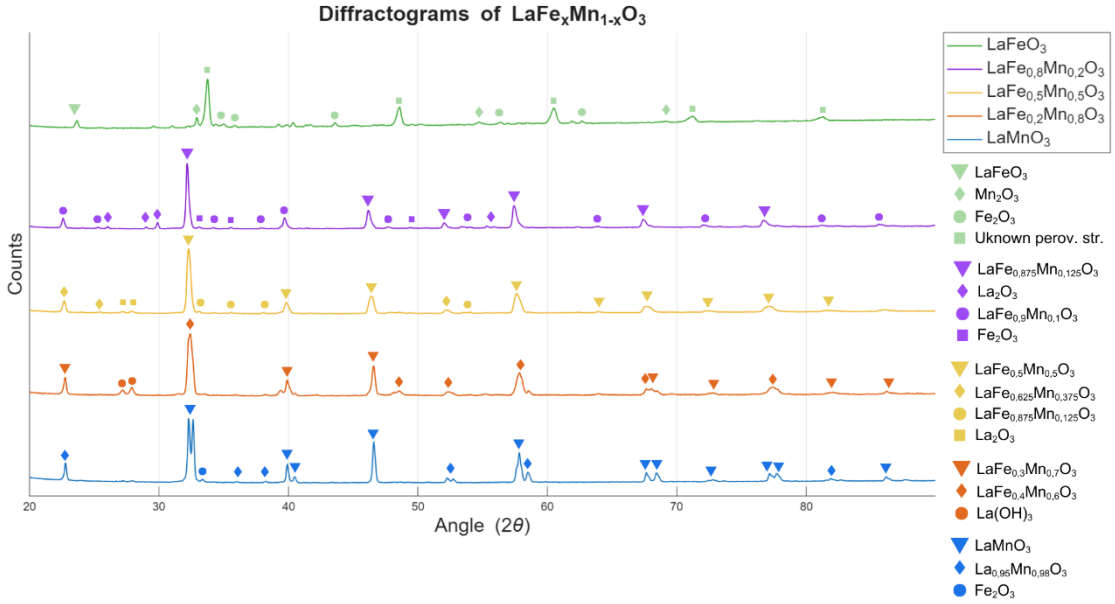

Figure 12: *Evolution of X-ray diffraction patterns for $LaFe_xMn_{1-x}O_{3-\delta}$ as a function of the iron composition (x = 1.0, 0.8, 0.5, 0.2, 0) forming $LaFeO_3$, $LaFe_{0.8}Mn_{0.2}O_3$, $LaFe_{0.5}Mn_{0.5}O_3$, $LaFe_{0.2}Mn_{0.8}O_3$ and $LaMnO_3$ going from top to bottom.*

The diffractogram reveals that the targeted $LaFeO_{3-\delta}$ is not the dominant phase, as the strong presence of Fe_2O_3 indicates incomplete formation. However, a perovskite fraction is clearly present, evidenced by five characteristic peaks found in the pattern. These peaks were misidentified by the software as $CdTiO_{3-\delta}$, also a perovskite structure, due to lattice distortions in the actual sample that prevented the correct reference recognition. The remaining unidentified peaks likely correspond to residual La- and Fe-oxide phases.

In the next diffractogram, demonstrates a highly successful formation of a $LaFe_xMn_{1-x}O_{3-\delta}$ solid solution, characterized by the presence of three nearly equivalent perovskite phases such as $LaFeO_3$ (32.3%), $La(Fe_{0.875}Mn_{0.125})O_3$ (31.5%), and $LaFe_{0.1}Mn_{0.9}O_3$ (31.9%), all with very high match scores. A minor La_2O_3 impurity (around 4.2%) is present but does not significantly affect the overall perovskite character.

Sample 8 is multiphase, but the analysis detects presence of $LaFe_{0.2}Mn_{0.8}O_3$ in the sample. The diffractogram contains $LaMnO_3$, $LaFeO_3$, and mixed $LaFe_xMn_{1-x}O_3$ phases with very high match scores (around 90–98%). This indicates partial solid-solution formation but also compositional segregation into Mn-rich and Fe-rich regions. All detected phases belong to the same perovskite family; however, it has been observed

some $La(OH)_3$ formed due to the exposure of moisture in the air in some point of the synthesis part.

The next diffractogram of $LaFe_{0.5}Mn_{0.5}O_{3-\delta}$ shows several $LaFe_xMn_{1-x}O_{3-\delta}$ compositions with high match scores (84–96%), consistent with the 1:1 Fe–Mn ratio. These phases form a continuous solid solution typical for $LaFe_xMn_{1-x}O_{3-\delta}$ systems. No unrelated impurities appear, reflecting good synthesis control, thus it matches the theoretical perovskite composition well, with only normal compositional variations.

The phases detected in the diffractogram of $LaMnO_{3-\delta}$ and closely related compositions such as $La_{0.91}Mn_{0.95}O_3$, $LaMn_{0.91}Fe_{0.1}O_3$ and $La_{0.95}Mn_{0.98}O_3$. $LaMnO_3$ is clearly the main phase, consistent with the target composition with a 92% of match, showing that the compound has good purity overall. Minor deviations suggest slight non-stoichiometry or Fe traces but also were chemically expected.

Figure 13 presents a summary of the amount of perovskite structure synthesized in each sample as a function of its composition.

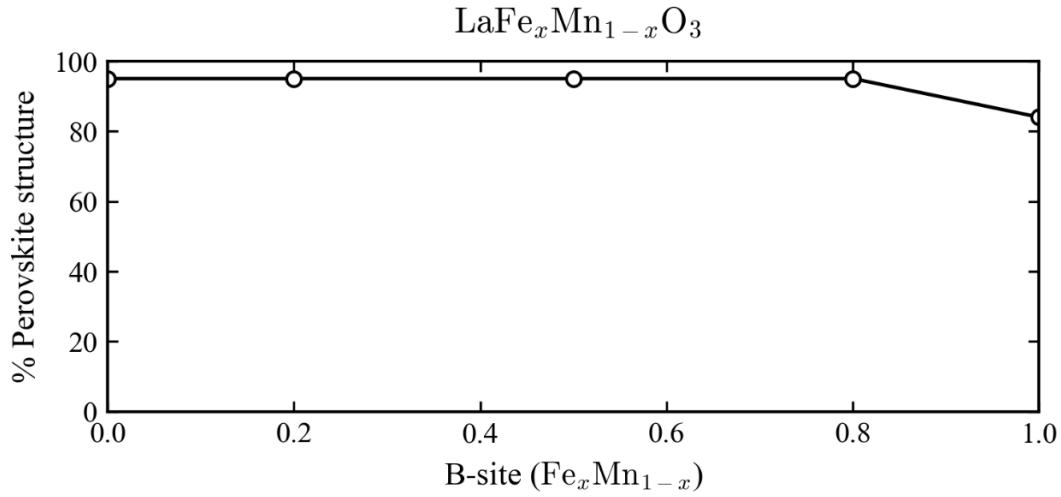

Figure 13: *Effect of B-site iron composition (x = 0, 0.2, 0.5, 0.8, 1.0) on the perovskite structure of $LaFe_xMn_{1-x}O_{3-\delta}$ forming $LaMnO_3$, $LaFe_{0.2}Mn_{0.8}O_3$, $LaFe_{0.5}Mn_{0.5}O_3$, $LaFe_{0.8}Mn_{0.2}O_3$ and $LaFeO_3$ going from left to right.*

5.2.3. Results in $Ca_xLa_{1-x}FeO_{3-\delta}$

The following figure details the structural analysis of samples of the $Ca_xLa_{1-x}FeO_{3-\delta}$ family, provided by the previous analyses of $CaFeO_3$ and $LaFeO_3$ parent compounds.

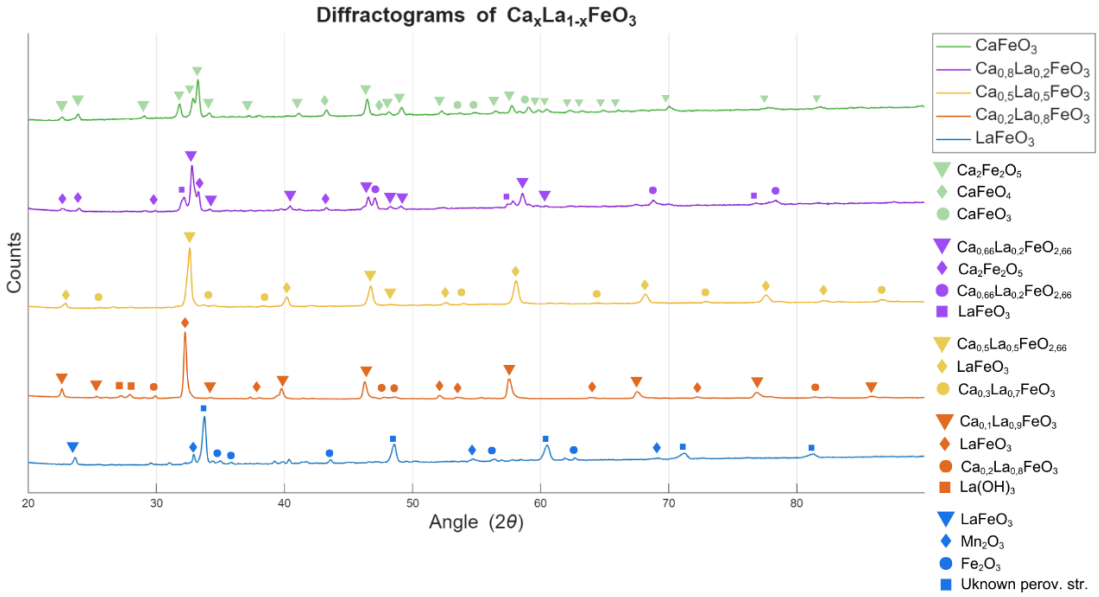

Figure 14: *Evolution of X-ray diffraction patterns for $Ca_xLa_{1-x}FeO_{3-\delta}$ as a function of the calcium composition (x = 1.0, 0.8, 0.5, 0.2, 0) forming $CaFeO_3$, $Ca_{0.8}La_{0.2}FeO_3$, $Ca_{0.5}La_{0.5}FeO_3$, $Ca_{0.2}La_{0.8}FeO_3$ and $LaFeO_3$ going from top to bottom.*

Regarding $Ca_{0.8}La_{0.2}FeO_{3-\delta}$ diffractogram, it indicates a significant departure from the target $Ca_xLa_{1-x}FeO_{3-\delta}$ perovskite. Instead of a single-phase structure, the material stabilized as a multiphase mixture dominated by layered and brownmillerite-type structures, notably $(LaCa_2Fe_3O_8)_{0,33}$ (~39.7%) and $Ca_2Fe_2O_5$ (~34.8%). The simultaneous presence of La-rich and Ca-rich oxide phases suggests poor compositional homogeneity and an incomplete solid-state reaction, resulting in strong phase segregation rather than a stabilized perovskite lattice.

Contrastingly, in $Ca_{0.2}La_{0.8}FeO_{3-\delta}$ demonstrates a successful synthesis of the intended composition. The identified phases consist of various Ca-doped $LaFeO_3$ variants (x = [0.1–0.2]), all of which are consistent with the perovskite structural family. While the sample exhibits mild compositional heterogeneity, the absence of foreign impurities confirms it is a high-quality representation of the targeted perovskite framework.

$Ca_{0.5}La_{0.5}FeO_{3-\delta}$ represents an intermediate state where, although all detected phases belong to the expected structural family, the system failed to reach chemical equilibrium. The sample is characterized by a mixture of several $Ca_xLa_{1-x}FeO_{3-\delta}$ compositions and $LaFeO_3$, indicating significant oxygen non-stoichiometry and internal inhomogeneity. Consequently, the material remains multiphase and does not fully achieve the theoretical uniformity of a single $Ca_{0.5}La_{0.5}FeO_{3-\delta}$ phase.

Figure 15 illustrates the correlation between the stoichiometric composition of the samples and the resulting yield of the perovskite crystalline phase.

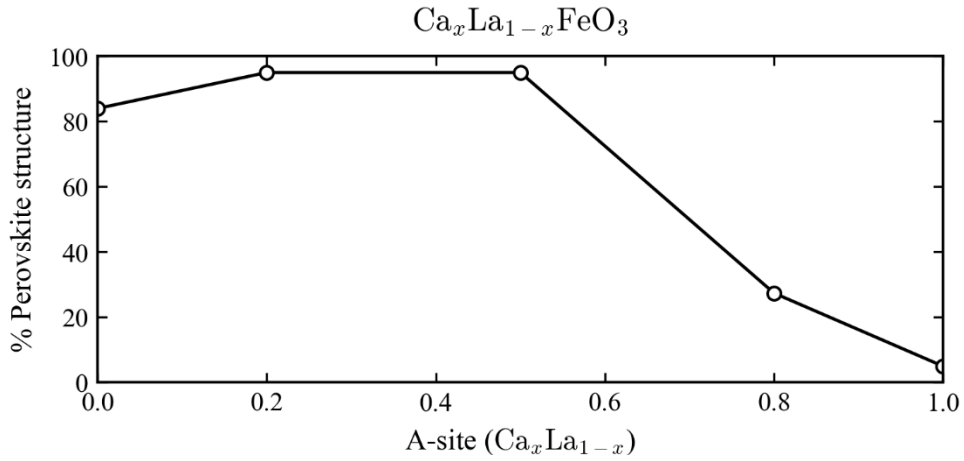

Figure 15: *Effect of A-site calcium composition (x = 0, 0.2, 0.5, 0.8, 1.0) on the perovskite structure of $Ca_xLa_{1-x}FeO_{3-\delta}$ forming $LaFeO_3$, $Ca_{0.2}La_{0.8}FeO_3$, $Ca_{0.5}La_{0.5}FeO_3$, $Ca_{0.8}La_{0.2}FeO_3$ and $CaFeO_3$ going from left to right.*

5.3. Thermogravimetric Analysis (TGA)

The redox behaviour was evaluated comparing the changes in oxygen non-stoichiometry (Δδ), which quantifies the moles of oxygen atoms released or incorporated per mole of perovskite (18). Firstly, $LaFeO_{3-\delta}$ sample was tested to evaluate its redox behavior under CO/CO_2 at different temperatures, specifically at 700, 800, and 900 °C.

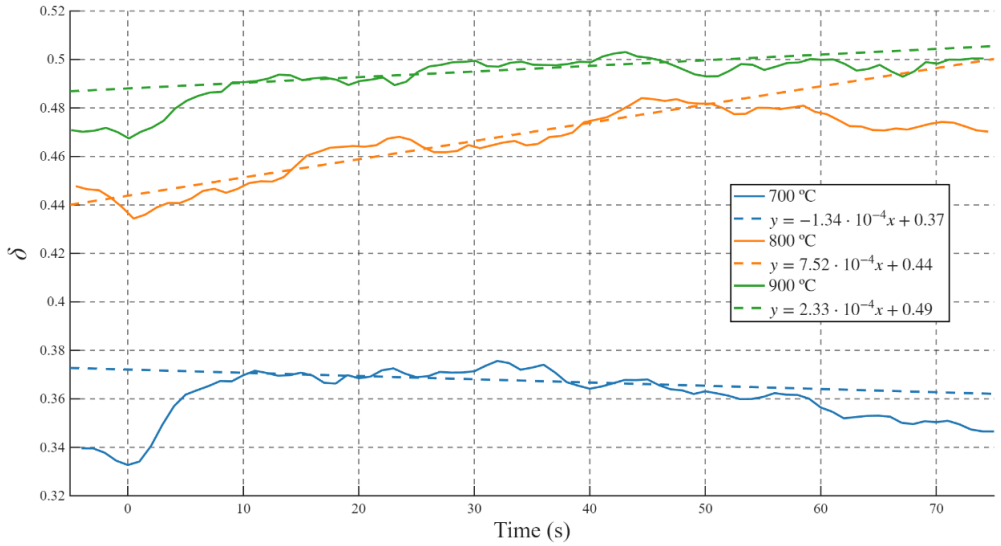

Figure 16: *Isothermal evolution of the oxygen non-stoichiometry (δ) in CO reduction over a 60-second interval at 700°C, 800°C, and 900°C using $LaFeO_{3-\delta}$ as a sample test.*

This specific sample was chosen as it showed good percentage of perovskite structure in the XRD analysis. During the reduction stage, it is observed that the largest mass loss and δ increase within the 60-second interval occurs at 800 °C. At 700 °C and 900 °C, δ increases sharply within only a few seconds, becoming difficult to control it, whereas at 800 °C the reduction proceeds more gradually and over a longer period. It is also noteworthy that, at 700 °C, the mass initially drops abruptly and then, contrary to what would be expected, begins to increase progressively (δ decreases). This behaviour may be attributed to carbon deposition on iron (7), a phenomenon commonly observed at this temperature. To prevent that, higher temperatures than 700 °C were chosen as it reduces significantly this risk.

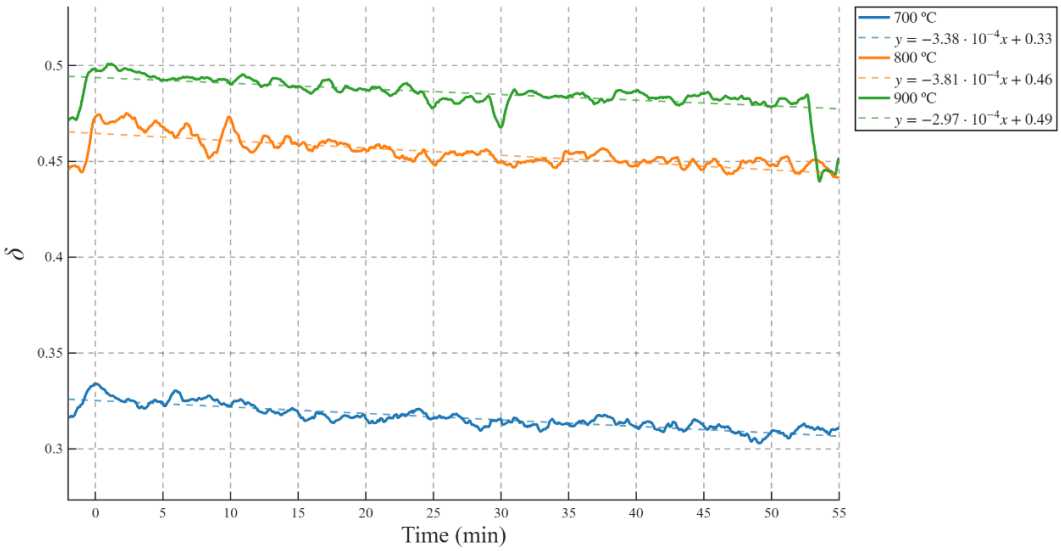

Figure 17: *Isothermal evolution of the oxygen non-stoichiometry (δ) in CO_2 oxidation over a 60-minute interval at 700°C, 800°C, and 900°C using $LaFeO_{3-\delta}$ as a sample test.*

Regarding the oxidation phase, reaction rates remained relatively consistent across the tested temperatures. Nevertheless, in distinct contrast to the reduction process, which occurs within seconds, the oxidation reaction exhibits significantly slower kinetics. Particularly, the oxidation reaction at 800°C achieved the highest mass recovery relative to the initial sample mass and the highest δ recovery during that process compared to the other isotherms.

Based on the optimal reactivity observed at 800°C, this temperature and its corresponding reaction intervals were selected as the standard operating parameters for the subsequent analysis of the samples, as this condition enabled the oxidation to recover mass more rapidly and efficiently compared with other tested temperatures.

Table 6 presents the evolution of δ across the specific stages of the thermogravimetric cycle. The calculations were performed using (18) and the data provided in Table 11.

The mass–time profiles obtained from the TGA experiments for all samples are presented in the Appendix.

Table 6: *Comparison of oxygen exchange capacities (Δδ) during a redox cycle for selected perovskites compositions and δ at the end of the cycle (δ_f)*

Sample	Compound	δ after heating	Δδ during CO red.	δ after reduction	Δδ during CO_2 Ox.	δ_f
S3	$LaMnO_{3-\delta}$	0.310	0.039	0.349	-0.019	0.330
S4	$LaFeO_{3-\delta}$	0.433	0.051	0.484	-0.049	0.435
S7	$CaFe_{0.5}Mn_{0.5}O_{3-\delta}$	0.245	0.024	0.269	-0.018	0.251
S10	$LaFe_{0.5}Mn_{0.5}O_{3-\delta}$	0.435	0.065	0.500	-0.029	0.471
S13	$Ca_{0.5}La_{0.5}FeO_{3-\delta}$	0.404	0.053	0.457	-0.041	0.416

The heating phase to 800°C revealed significant differences in the oxygen lattice stability. Sample 4 and Sample 10 exhibited the highest oxygen loss during heating, reaching Δδ values of 0.433 and 0.435, respectively. This suggests a lower formation energy for oxygen vacancies in these iron-containing structures compared to Sample 3.

In contrast, the substitution of lanthanum with calcium in Sample 7 resulted in a more thermally stable lattice, with a significantly lower Δδ of 0.024 during the reduction phase and with δ after heating with a value of 0.245. This indicates that Ca^{2+} substitution in the A-site, combined with the mix in the B-site of manganese and iron, could effectively prevent the release of lattice oxygen under increasing temperature.

Upon introduction of CO at 800 °C, further mass loss was observed in all samples, although to a lesser extent than during heating. Sample 10 and Sample 13 showed the highest reactivity towards the reducing agent (approx. 0.05-0.06), while Sample 3 appeared nearly saturated after the heating phase, showing minimal additional reduction of 0.039.

In the oxidation phase, the data shows that Sample 4 outperformed comparing to the other compounds. While $LaMnO_{3-\delta}$ recovered 0.019 in δ and $CaFe_{0.5}Mn_{0.5}O_{3-\delta}$ only 0.018, the mixed B-site configuration in Sample 4 achieved a recovery of 0.049. This suggests a synergistic effect where the presence of both Fe and Mn ions may enhance the surface exchange kinetics and the thermodynamic drive for CO_2 dissociation.

Sample 13 also exhibited an oxidation capacity of 0.041, the second highest, indicating that A-site substitution with calcium could improve the re-oxidation kinetics of ferrite-based perovskites. In fact, calcium seems to contribute to thermal stability, while iron

and lanthanum maintain the fast oxidation kinetics required for efficient hydrogen production, making a very equilibrated sample. Nevertheless, Sample 7, despite its stability during heating, showed the lowest oxidation performance about 0.018, suggesting that while the lattice is more stable, it is also less kinetically active for CO_2 splitting under these specific isothermal conditions.

Observing the slope of the mass gain during the CO_2 oxidation phase, Samples 10 and 13 show a sharper initial weight gain compared to Sample 7. This sample displays a very shallow slope, which points toward a high activation energy or slow surface reaction rate for CO_2 splitting. The combination of the elements on the B and A sites of Fe and Mn or Ca and La respectively appears to overcome these kinetic limitations, allowing for a more rapid approach to the stoichiometric equilibrium within the 90-minute window.

To sum up, Sample 10 and Sample 4 are the ones that show better OEC as they have the highest δ value. Nevertheless, Sample 10 in the reduction had a δ of 0.5 and also sample 4 near that value, so Sample 10 was considered not suitable. Sample 13 showed exceptional CO_2 splitting performance and the second highest oxygen recovery value among all synthesized materials. It performs better than $LaFeO_3$ because the optimized mix of Fe and Mn creates a strong synergistic effect. It can undergo significant thermal and chemical reduction, producing many oxygen vacancies that boost its redox activity. During oxidation, it reacts the fastest, quickly taking up oxygen from CO_2.

From a larger-scale or industrial perspective, when comparing Sample 4 and Sample 13, the balance clearly favors the latter. $Ca_{0.5}La_{0.5}FeO_{3-\delta}$ combines the high kinetics of Fe with the thermal and structural stability provided by Ca and La, thereby mitigating the sintering and degradation issues commonly associated with traditional iron oxides. These characteristics result in Sample 13 ($Ca_{0.5}La_{0.5}FeO_{3-\delta}$) being a well-balanced oxygen carrier.

Also, from an economic standpoint, the partial substitution of La with Ca significantly reduces material costs, as Ca is considerably less expensive than La. Table 7 and Table 8 showed that by substituting 50% of the Lanthanum with Calcium, the raw material cost is reduced by approximately 30%. The prices of lanthanum(III), iron(III) and calcium oxides were extracted from [29], [30] and [31] respectively.

Table 7: *Cost of raw material analysis for Sample 4 - $LaFeO_{3-\delta}$*

Final product	Precursor	Mass used (g)	Unit Price (€/kg)	Cost (€)	Cost per gram of OC (€/g)
$LaFeO_{3-\delta}$	La_2O_3	3.4	943.63	3.208	0.706
	Fe_2O_3	1.6	201.85	0.323	
			TOTAL COST	3.531	

Table 8: *Cost of raw material analysis for Sample 13 - $Ca_{0.5}La_{0.5}FeO_{3-\delta}$*

Final product	Precursor	Mass used (g)	Unit Price (€/kg)	Cost (€)	Cost per gram of OC (€/g)
$Ca_{0.5}La_{0.5}FeO_{3-\delta}$	CaO	0.7	35.63	0.025	0.496
	La_2O_3	2.1	943.63	1.982	
	Fe_2O_3	2.1	201.85	0.424	
			TOTAL COST	1.817	

Given these advantages, Sample 13 outperforms Sample 4 and holds more industrial promise for the chemical sector.

6. Conclusion

In this master thesis, it was investigated the synthesis, structural stability and redox performance of a series of perovskite-type oxides with the aim of determining their suitability as oxygen carriers for Chemical Looping Water Splitting. The experimental results allow clear answers to each of the initial objectives and research questions set in the beginning.

XRD analysis confirmed that manganate-based perovskites, specifically $CaMnO_{3-\delta}$ (Sample 1) and $LaMnO_{3-\delta}$ (Sample 3), achieved the highest structural fidelity, with experimental peaks aligning closely with standard reference patterns of perovskites in the databases. Synthesis also worked with most of the perovskites that had complex A and B site mixtures with different elements. Contrastingly, the synthesis of $CaFeO_{3-\delta}$ resulted in incomplete stabilization, often coexisting with secondary phases such as brownmillerite ($Ca_2Fe_2O_5$) or other iron oxides. Other ferrites such as $LaFeO_{3-\delta,}$ despite not being completely pure as well as $CaFeO_{3-\delta,}$ it managed to develop perovskite structure. Thus, it has been successfully established a reproductible synthesis methodology that is effective in order to create perovskite phase, specially with manganese-based and complex mixtures.

The thesis demonstrated that personalising the perovskite lattice through ionic substitution significantly impacts phase stability and reaction kinetics. For example, replacing calcium with lanthanum in Sample 10 ($LaFe_{0.5}Mn_{0.5}O_{3-\delta}$) created a more thermally stable lattice during heating and resulted in the highest oxidation performance during the CO_2 splitting phase, following Sample 4. Nevertheless, they were no considered as suitable OEC due to their proximity to the δ=0.5 limit.

Moreover, TGA revealed that oxygen exchange capacity is highly sensitive to the material's stoichiometry. Iron-containing structures (Samples 4 and 10) exhibited the highest oxygen loss during heating, indicating a lower formation energy for vacancies. On the other hand, A-site substitution with calcium in Sample 7 enhanced thermal stability but reduced the kinetics of CO_2 splitting.

In the end, Sample 13 ($Ca_{0.5}La_{0.5}FeO_{3-\delta}$) was identified as the most suitable oxygen carrier. It outperformed pure $LaMnO_3$, winning them in oxidation rate and flexible structure and beats Sample 4, due to its flexible structure and highly reactive surface, make it a potential candidate for hydrogen generation in Steam-iron processes and in big industry processes.

Bibliography

[1] H. C. de, 'IPCC Special Report on Carbon Dioxide Capture and Storage'.

[2] K. Calvin *et al.*, 'IPCC, 2023: Climate Change 2023: Synthesis Report. Contribution of Working Groups I, II and III to the Sixth Assessment Report of the Intergovernmental Panel on Climate Change [Core Writing Team, H. Lee and J. Romero (eds.)]. IPCC, Geneva, Switzerland.', Intergovernmental Panel on Climate Change (IPCC), Jul. 2023. doi: 10.59327/IPCC/AR6-9789291691647.

[3] I. Rolo, V. A. F. Costa, F. P. Brito, I. Rolo, V. A. F. Costa, and F. P. Brito, 'Hydrogen-Based Energy Systems: Current Technology Development Status, Opportunities and Challenges', *Energies*, vol. 17, no. 1, Dec. 2023, doi: 10.3390/en17010180.

[4] 'Global Hydrogen Review 2023', 2023.

[5] A. Hauch *et al.*, 'Recent advances in solid oxide cell technology for electrolysis', *Science*, vol. 370, no. 6513, p. eaba6118, Oct. 2020, doi: 10.1126/science.aba6118.

[6] T. Renzelmann, 'DEGREE PROJECT IN SUSTAINABLE ENERGY ENGINEERING SECOND CYCLE, 30 CREDITS'.

[7] M. F. Ahmad Kamaroddin *et al.*, 'Membrane-Based Electrolysis for Hydrogen Production: A Review', *Membranes*, vol. 11, no. 11, p. 810, Oct. 2021, doi: 10.3390/membranes11110810.

[8] D. Kunii and O. Levenspiel, *Fluidization engineering*, 2. ed., Reprinted. in Butterworth-Heinemann series in chemical engineering. Amsterdam Heidelberg: Elsevier ; Butterworth-Heinemann, 2012.

[9] P. Basu, *Combustion and gasification in fluidized beds*. Boca Raton: CRC, Taylor & Francis, 2006.

[10] A. Gyllén, 'Oxygen Carrier Aided Combustion: Implementation of Oxygen Carriers to Existing Industrial Settings', Ph.D., 2019. Accessed: Dec. 29, 2025. [Online]. Available: https://www.proquest.com/docview/2316054248/abstract/4AFAFFCD6C834721PQ/1

[11] A. Messerschmitt, O. Frankfort-On-Tfe-Main, and O. Frankfort-On-The-Main, 'UNITED STATES PATENT OFFICE.'.

[12] V. Hacker, H. Fuchs, M. Muhr, and K. Friedrich, 'The steam-iron process for gas reforming and hydrogen generation: Fuel Cell Seminar', *Fuel Cell Seminar*, pp. 333–335, 2000.

[13] M. Rydén and M. Arjmand, 'Continuous hydrogen production via the steam–iron reaction by chemical looping in a circulating fluidized-bed reactor', *International Journal of Hydrogen Energy*, vol. 37, no. 6, pp. 4843–4854, Mar. 2012, doi: 10.1016/j.ijhydene.2011.12.037.

[14] E. Schürmann and U. Janhsen, 'Determination of the phase boundaries of the wustite solid solution within the context of reduction tests', *Steel Research*, vol. 64, no. 6, pp. 279–285, 1993, doi: 10.1002/srin.199301023.

[15] J. Hunt, A. Ferrari, A. Lita, M. Crosswhite, B. Ashley, and A. E. Stiegman, 'Microwave-Specific Enhancement of the Carbon–Carbon Dioxide (Boudouard)

Reaction', *J. Phys. Chem. C*, vol. 117, no. 51, pp. 26871–26880, Dec. 2013, doi: 10.1021/jp4076965.
[16] A. Lyngfelt and C. Linderholm, 'Chemical-Looping Combustion of Solid Fuels – Status and Recent Progress', *Energy Procedia*, vol. 114, pp. 371–386, Jul. 2017, doi: 10.1016/j.egypro.2017.03.1179.
[17] F. García-Labiano, L. F. de Diego, J. Adánez, A. Abad, and P. Gayán, 'Temperature variations in the oxygen carrier particles during their reduction and oxidation in a chemical-looping combustion system', *Chemical Engineering Science*, vol. 60, no. 3, pp. 851–862, Feb. 2005, doi: 10.1016/j.ces.2004.09.049.
[18] L.-S. Fan, *Chemical Looping Systems for Fossil Energy Conversions*. John Wiley & Sons, 2011.
[19] 'Recent advancements in chemical looping water splitting for the production of hydrogen - RSC Advances (RSC Publishing) DOI:10.1039/C6RA21180A'. Accessed: Dec. 29, 2025. [Online]. Available: https://pubs.rsc.org/en/content/articlehtml/2016/ra/c6ra21180a
[20] 'Chemical looping combustion (CLC)', in *Fluidized Bed Technologies for Near-Zero Emission Combustion and Gasification*, Woodhead Publishing, 2013, pp. 895–930. doi: 10.1533/9780857098801.4.895.
[21] K. Wang, C. Han, Z. Shao, J. Qiu, S. Wang, and S. Liu, 'Perovskite Oxide Catalysts for Advanced Oxidation Reactions', *Adv Funct Materials*, vol. 31, no. 30, p. 2102089, Jul. 2021, doi: 10.1002/adfm.202102089.
[22] F. S. Galasso, *Structure, Properties and Preparation of Perovskite-Type Compounds: International Series of Monographs in Solid State Physics*. Elsevier, 2013.
[23] Z. Li, M. Yang, J.-S. Park, S.-H. Wei, J. J. Berry, and K. Zhu, 'Stabilizing Perovskite Structures by Tuning Tolerance Factor: Formation of Formamidinium and Cesium Lead Iodide Solid-State Alloys', *Chem. Mater.*, vol. 28, no. 1, pp. 284–292, Jan. 2016, doi: 10.1021/acs.chemmater.5b04107.
[24] M. Lallart, *Ferroelectrics: Physical Effects*. BoD – Books on Demand, 2011.
[25] S. E. Dann, *Reactions and Characterization of Solids*. Royal Society of Chemistry, 2000.
[26] C.-12 Foundation, 'Wave Interference | CK-12 Foundation'. Accessed: Dec. 29, 2025. [Online]. Available: https://flexbooks.ck12.org/cbook/ck-12-physics-flexbook-2.0/section/11.5/primary/lesson/wave-interference-ms-ps/
[27] Y. A. Daza, R. A. Kent, M. M. Yung, and J. N. Kuhn, 'Carbon Dioxide Conversion by Reverse Water–Gas Shift Chemical Looping on Perovskite-Type Oxides', *Ind. Eng. Chem. Res.*, vol. 53, no. 14, pp. 5828–5837, Apr. 2014, doi: 10.1021/ie5002185.
[28] F. R. Valli, 'Experimental analysis of CO2 splitting by perovskites-based Chemical Looping: isothermal redox cycling of SFNM-04 in a microreactor setup', laurea, Politecnico di Torino, 2022. Accessed: Dec. 29, 2025. [Online]. Available: https://webthesis.biblio.polito.it/22126/
[29] 'Lanthanum(III) oxide 99.99 trace metals 1312-81-8'. Accessed: Jan. 26, 2026. [Online]. Available: https://www.sigmaaldrich.com/SE/en/product/aldrich/199923

[30] ‘Iron(III) oxide, 98% (metals basis), Thermo Scientific Chemicals 5 kg | Contact Us’. Accessed: Jan. 26, 2026. [Online]. Available: https://www.thermofisher.com/order/catalog/product/012375.A7
[31] ‘Calcium oxide, 97+%, for analysis, powder 1 kg | Buy Online | Thermo Scientific Chemicals’. Accessed: Jan. 26, 2026. [Online]. Available: https://www.thermofisher.com/order/catalog/product/422830010

7.Appendix

7.1. Tables

Table 9: *Stoichiometric Reaction Formulas for Samples 1 to 13*

Sample	Reaction formula	
1	$2CaO + Mn_2O_3 + 0.5O_2 \rightarrow 2CaMnO_3$	(23)
2	$2CaO + Fe_2O_3 + 0.5O_2 \rightarrow 2CaFeO_3$	(24)
3	$La_2O_3 + Mn_2O_3 \rightarrow 2LaMnO_3$	(25)
4	$La_2O_3 + Fe_2O_3 \rightarrow 2LaFeO_3$	(26)
5	$10CaO + Fe_2O_3 + 4Mn_2O_3 + 2.5O_2 \rightarrow 10CaFe_{0.2}Mn_{0.8}O_3$	(27)
6	$10CaO + 4Fe_2O_3 + Mn_2O_3 + 2.5O_2 \rightarrow 10CaFe_{0.8}Mn_{0.2}O_3$	(28)
7	$4CaO + Fe_2O_3 + Mn_2O_3 + O_2 \rightarrow 10CaFe_{0.5}Mn_{0.5}O_3$	(29)
8	$5La_2O_3 + Fe_2O_3 + 4Mn_2O_3 \rightarrow 10LaFe_{0.2}Mn_{0.8}O_3$	(30)
9	$5La_2O_3 + 4Fe_2O_3 + Mn_2O_3 \rightarrow 10LaFe_{0.8}Mn_{0.2}O_3$	(31)
10	$2La_2O_3 + Fe_2O_3 + Mn_2O_3 \rightarrow 4LaFe_{0.5}Mn_{0.5}O_3$	(32)
11	$CaO + 2La_2O_3 + 2{,}5Fe_2O_3 + 0.25O_2 \rightarrow 5Ca_{0.2}La_{0.8}FeO_3$	(33)
12	$8CaO + La_2O_3 + 5Fe_2O_3 + 3O_2 \rightarrow 10Ca_{0.8}La_{0.2}FeO_3$	(34)
13	$2CaO + La_2O_3 + 2Fe_2O_3 + 0.5O_2 \rightarrow 4Ca_{0.5}La_{0.5}FeO_3$	(35)

Table 10: *Formulas used for calculating the masses of the precursor compounds from sample 1 to 13*

Sample	Formulas	
1	$m_{Mn_2O_3} = \frac{2g\ of\ CaO}{molar\ mass\ of\ CaO\left[\frac{g}{mole}\right]} * \frac{1\ mole\ of\ Mn_2O_3}{2\ moles\ of\ CaO} * \frac{molar\ mass\ of\ Mn_2O_3\left[\frac{g}{mole}\right]}{1\ mole\ of\ Mn_2O_3}$	(36)
2	$m_{CaO} = \frac{5g\ of\ product}{molar\ mass\ of\ product\left[\frac{g}{mole}\right]} * \frac{1\ mole\ of\ CaO}{1\ mole\ of\ product} * \frac{molar\ mass\ of\ CaO\left[\frac{g}{mole}\right]}{1\ mole\ of\ CaO}$	(37)
	$m_{Fe_2O_3} = \frac{5g\ of\ product}{molar\ mass\ of\ product\left[\frac{g}{mole}\right]} * \frac{1\ mole\ of\ Fe_2O_3}{2\ moles\ of\ product} * \frac{molar\ mass\ of\ Fe_2O_3\left[\frac{g}{mole}\right]}{1\ mole\ of\ Fe_2O_3}$	(38)
3	$m_{La_2O_3} = \frac{5g\ of\ product}{molar\ mass\ of\ product\left[\frac{g}{mole}\right]} * \frac{1\ mole\ of\ La_2O_3}{2\ moles\ of\ product} * \frac{molar\ mass\ of\ La_2O_3\left[\frac{g}{mole}\right]}{1\ mole\ of\ La_2O_3}$	(39)
	$m_{Mn_2O_3} = \frac{5g\ of\ product}{molar\ mass\ of\ product\left[\frac{g}{mole}\right]} * \frac{1\ mole\ of\ Mn_2O_3}{2\ moles\ of\ product} * \frac{molar\ mass\ of\ Mn_2O_3\left[\frac{g}{mole}\right]}{1\ mole\ of\ Mn_2O_3}$	(40)

4	$m_{La_2O_3} = \frac{5g\ of\ product}{molar\ mass\ of\ product\left[\frac{g}{mole}\right]} * \frac{1\ mole\ of\ La_2O_3}{2\ moles\ of\ product} * \frac{molar\ mass\ of\ La_2O_3\left[\frac{g}{mole}\right]}{1\ mole\ of\ La_2O_3}$	(41)
	$m_{Fe_2O_3} = \frac{5g\ of\ product}{molar\ mass\ of\ product\left[\frac{g}{mole}\right]} * \frac{1\ mole\ of\ Fe_2O_3}{2\ moles\ of\ product} * \frac{molar\ mass\ of\ Fe_2O_3\left[\frac{g}{mole}\right]}{1\ mole\ of\ Fe_2O_3}$	(42)
5	$m_{CaO} = \frac{5g\ of\ product}{molar\ mass\ of\ product\left[\frac{g}{mole}\right]} * \frac{1\ mole\ of\ CaO}{1\ mole\ of\ product} * \frac{molar\ mass\ of\ CaO\left[\frac{g}{mole}\right]}{1\ mole\ of\ CaO}$	(43)
	$m_{Fe_2O_3} = \frac{5g\ of\ product}{molar\ mass\ of\ product\left[\frac{g}{mole}\right]} * \frac{1\ mole\ of\ Fe_2O_3}{10\ moles\ of\ product} * \frac{molar\ mass\ of\ Fe_2O_3\left[\frac{g}{mole}\right]}{1\ mole\ of\ Fe_2O_3}$	(44)
	$m_{Mn_2O_3} = \frac{5g\ of\ product}{molar\ mass\ of\ product\left[\frac{g}{mole}\right]} * \frac{2\ moles\ of\ Mn_2O_3}{5\ moles\ of\ product} * \frac{molar\ mass\ of\ Mn_2O_3\left[\frac{g}{mole}\right]}{1\ mole\ of\ Mn_2O_3}$	(45)
6	$m_{CaO} = \frac{5g\ of\ product}{molar\ mass\ of\ product\left[\frac{g}{mole}\right]} * \frac{1\ mole\ of\ CaO}{1\ mole\ of\ product} * \frac{molar\ mass\ of\ CaO\left[\frac{g}{mole}\right]}{1\ mole\ of\ CaO}$	(46)
	$m_{Fe_2O_3} = \frac{5g\ of\ product}{molar\ mass\ of\ product\left[\frac{g}{mole}\right]} * \frac{2\ mole\ of\ Fe_2O_3}{5\ moles\ of\ product} * \frac{molar\ mass\ of\ Fe_2O_3\left[\frac{g}{mole}\right]}{1\ mole\ of\ Fe_2O_3}$	(47)
	$m_{Mn_2O_3} = \frac{5g\ of\ product}{molar\ mass\ of\ product\left[\frac{g}{mole}\right]} * \frac{1\ mole\ of\ Mn_2O_3}{10\ moles\ of\ product} * \frac{molar\ mass\ of\ Mn_2O_3\left[\frac{g}{mole}\right]}{1\ mole\ of\ Mn_2O_3}$	(48)
7	$m_{CaO} = \frac{5g\ of\ product}{molar\ mass\ of\ product\left[\frac{g}{mole}\right]} * \frac{1\ mole\ of\ CaO}{1\ mole\ of\ product} * \frac{molar\ mass\ of\ CaO\left[\frac{g}{mole}\right]}{1\ mole\ of\ CaO}$	(49)
	$m_{Fe_2O_3} = \frac{5g\ of\ product}{molar\ mass\ of\ product\left[\frac{g}{mole}\right]} * \frac{1\ mole\ of\ Fe_2O_3}{4\ moles\ of\ product} * \frac{molar\ mass\ of\ Fe_2O_3\left[\frac{g}{mole}\right]}{1\ mole\ of\ Fe_2O_3}$	(50)
	$m_{Mn_2O_3} = \frac{5g\ of\ product}{molar\ mass\ of\ product\left[\frac{g}{mole}\right]} * \frac{1\ mole\ of\ Mn_2O_3}{4\ moles\ of\ product} * \frac{molar\ mass\ of\ Mn_2O_3\left[\frac{g}{mole}\right]}{1\ mole\ of\ Mn_2O_3}$	(51)
8	$m_{La_2O_3} = \frac{5g\ of\ product}{molar\ mass\ of\ product\left[\frac{g}{mole}\right]} * \frac{1\ mole\ of\ La_2O_3}{2\ moles\ of\ product} * \frac{molar\ mass\ of\ La_2O_3\left[\frac{g}{mole}\right]}{1\ mole\ of\ La_2O_3}$	(52)
	$m_{Fe_2O_3} = \frac{5g\ of\ product}{molar\ mass\ of\ product\left[\frac{g}{mole}\right]} * \frac{1\ mole\ of\ Fe_2O_3}{10\ moles\ of\ product} * \frac{molar\ mass\ of\ Fe_2O_3\left[\frac{g}{mole}\right]}{1\ mole\ of\ Fe_2O_3}$	(53)
	$m_{Mn_2O_3} = \frac{5g\ of\ product}{molar\ mass\ of\ product\left[\frac{g}{mole}\right]} * \frac{2\ moles\ of\ Mn_2O_3}{5\ moles\ of\ product} * \frac{molar\ mass\ of\ Mn_2O_3\left[\frac{g}{mole}\right]}{1\ mole\ of\ Mn_2O_3}$	(54)
9	$m_{La_2O_3} = \frac{5g\ of\ product}{molar\ mass\ of\ product\left[\frac{g}{mole}\right]} * \frac{1\ mole\ of\ La_2O_3}{2\ moles\ of\ product} * \frac{molar\ mass\ of\ La_2O_3\left[\frac{g}{mole}\right]}{1\ mole\ of\ La_2O_3}$	(55)
	$m_{Fe_2O_3} = \frac{5g\ of\ product}{molar\ mass\ of\ product\left[\frac{g}{mole}\right]} * \frac{2\ moles\ of\ Fe_2O_3}{5\ moles\ of\ product} * \frac{molar\ mass\ of\ Fe_2O_3\left[\frac{g}{mole}\right]}{1\ mole\ of\ Fe_2O_3}$	(56)
	$m_{Mn_2O_3} = \frac{5g\ of\ product}{molar\ mass\ of\ product\left[\frac{g}{mole}\right]} * \frac{1\ mole\ of\ Mn_2O_3}{10\ moles\ of\ product} * \frac{molar\ mass\ of\ Mn_2O_3\left[\frac{g}{mole}\right]}{1\ mole\ of\ Mn_2O_3}$	(57)
10	$m_{La_2O_3} = \frac{5g\ of\ product}{molar\ mass\ of\ product\left[\frac{g}{mole}\right]} * \frac{1\ mole\ of\ La_2O_3}{2\ moles\ of\ product} * \frac{molar\ mass\ of\ La_2O_3\left[\frac{g}{mole}\right]}{1\ mole\ of\ La_2O_3}$	(58)
	$m_{Fe_2O_3} = \frac{5g\ of\ product}{molar\ mass\ of\ product\left[\frac{g}{mole}\right]} * \frac{1\ mole\ of\ Fe_2O_3}{4\ moles\ of\ product} * \frac{molar\ mass\ of\ Fe_2O_3\left[\frac{g}{mole}\right]}{1\ mole\ of\ Fe_2O_3}$	(59)

	$m_{Mn_2O_3} = \frac{5g\ of\ product}{molar\ mass\ of\ product\left[\frac{g}{mole}\right]} * \frac{1\ mole\ of\ Mn_2O_3}{4\ moles\ of\ product} * \frac{molar\ mass\ of\ Mn_2O_3\left[\frac{g}{mole}\right]}{1\ mole\ of\ Mn_2O_3}$	(60)
11	$m_{CaO} = \frac{5g\ of\ product}{molar\ mass\ of\ product\left[\frac{g}{mole}\right]} * \frac{1\ mole\ of\ CaO}{5\ mole\ of\ product} * \frac{molar\ mass\ of\ CaO\left[\frac{g}{mole}\right]}{1\ mole\ of\ CaO}$	(61)
	$m_{La_2O_3} = \frac{5g\ of\ product}{molar\ mass\ of\ product\left[\frac{g}{mole}\right]} * \frac{2\ mole\ of\ La_2O_3}{5\ moles\ of\ product} * \frac{molar\ mass\ of\ La_2O_3\left[\frac{g}{mole}\right]}{1\ mole\ of\ La_2O_3}$	(62)
	$m_{Fe_2O_3} = \frac{5g\ of\ product}{molar\ mass\ of\ product\left[\frac{g}{mole}\right]} * \frac{2\ moles\ of\ Fe_2O_3}{1\ mole\ of\ product} * \frac{molar\ mass\ of\ Fe_2O_3\left[\frac{g}{mole}\right]}{1\ mole\ of\ Fe_2O_3}$	(63)
12	$m_{CaO} = \frac{5g\ of\ product}{molar\ mass\ of\ product\left[\frac{g}{mole}\right]} * \frac{8\ mole\ of\ CaO}{10\ mole\ of\ product} * \frac{molar\ mass\ of\ CaO\left[\frac{g}{mole}\right]}{1\ mole\ of\ CaO}$	(64)
	$m_{La_2O_3} = \frac{5g\ of\ product}{molar\ mass\ of\ product\left[\frac{g}{mole}\right]} * \frac{1\ mole\ of\ La_2O_3}{10\ moles\ of\ product} * \frac{molar\ mass\ of\ La_2O_3\left[\frac{g}{mole}\right]}{1\ mole\ of\ La_2O_3}$	(65)
	$m_{Fe_2O_3} = \frac{5g\ of\ product}{molar\ mass\ of\ product\left[\frac{g}{mole}\right]} * \frac{1\ moles\ of\ Fe_2O_3}{2\ mole\ of\ product} * \frac{molar\ mass\ of\ Fe_2O_3\left[\frac{g}{mole}\right]}{1\ mole\ of\ Fe_2O_3}$	(66)
13	$m_{CaO} = \frac{5g\ of\ product}{molar\ mass\ of\ product\left[\frac{g}{mole}\right]} * \frac{1\ mole\ of\ CaO}{2\ moles\ of\ product} * \frac{molar\ mass\ of\ CaO\left[\frac{g}{mole}\right]}{1\ mole\ of\ CaO}$	(67)
	$m_{La_2O_3} = \frac{5g\ of\ product}{molar\ mass\ of\ product\left[\frac{g}{mole}\right]} * \frac{1\ mole\ of\ La_2O_3}{4\ moles\ of\ product} * \frac{molar\ mass\ of\ La_2O_3\left[\frac{g}{mole}\right]}{1\ mole\ of\ La_2O_3}$	(68)
	$m_{Fe_2O_3} = \frac{5g\ of\ product}{molar\ mass\ of\ product\left[\frac{g}{mole}\right]} * \frac{1\ mole\ of\ Fe_2O_3}{2\ moles\ of\ product} * \frac{molar\ mass\ of\ Fe_2O_3\left[\frac{g}{mole}\right]}{1\ mole\ of\ Fe_2O_3}$	(69)

Table 11: *Experimental initial and final masses measurements of each sample during reduction and oxidation cycles*

Sample	Compound	Mass (mg)	Reduction	Oxidation	M_{ABO3}
S3	$LaMnO_{3-\delta}$	m_0	18.1519	18.1046	241.84
		m_f	18.1046	18.1269	
S4	$LaFeO_{3-\delta}$	m_0	18.3862	18.3242	242.75
		m_f	18.3242	18.3833	
S7	$CaFe_{0.5}Mn_{0.5}O_{3-\delta}$	m_0	17.8417	17.7941	143.47
		m_f	17.7941	17.8302	
S10	$LaFe_{0.5}Mn_{0.5}O_{3-\delta}$	m_0	16.2612	16.1918	242.29
		m_f	16.1918	16.2226	
S13	$Ca_{0.5}La_{0.5}FeO_{3-\delta}$	m_0	15.8926	15.8229	193.33
		m_f	15.8229	15.8765	

7.2. Sample diffractograms

7.2.1. Sample 1 – $CaMnO_{3-\delta}$

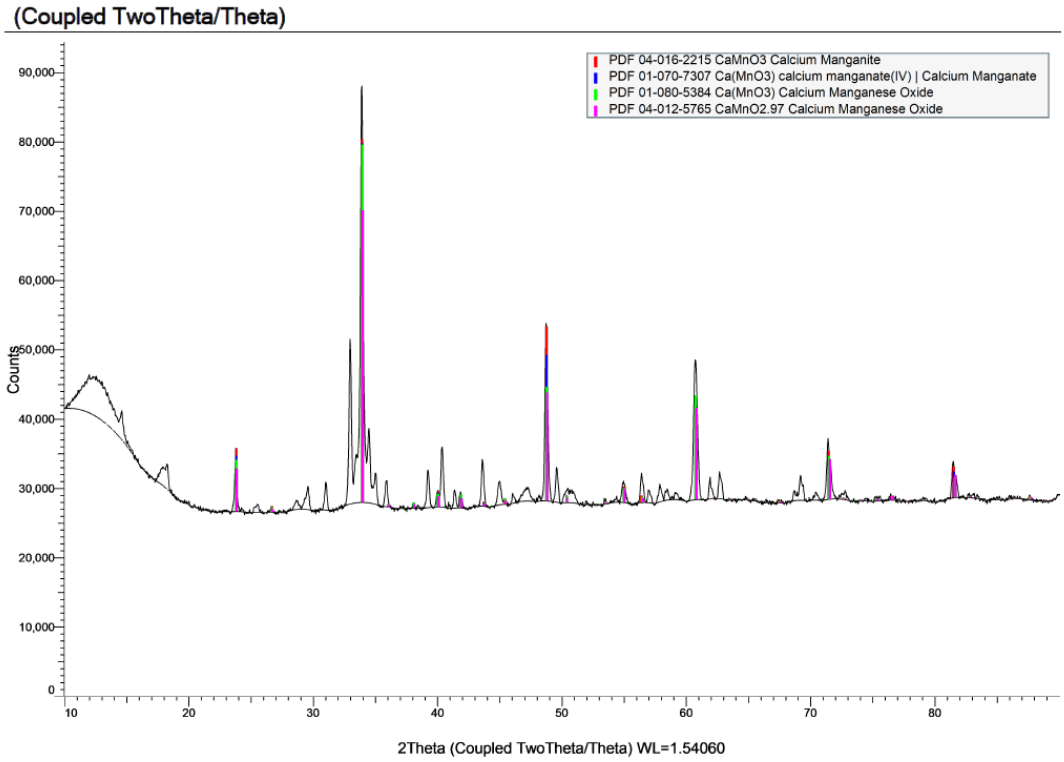

Figure 18: *X-ray diffraction analysis of Sample 1.5 showing peak matches with $CaMnO_{3-\delta}$ and related perovskite oxide phases*

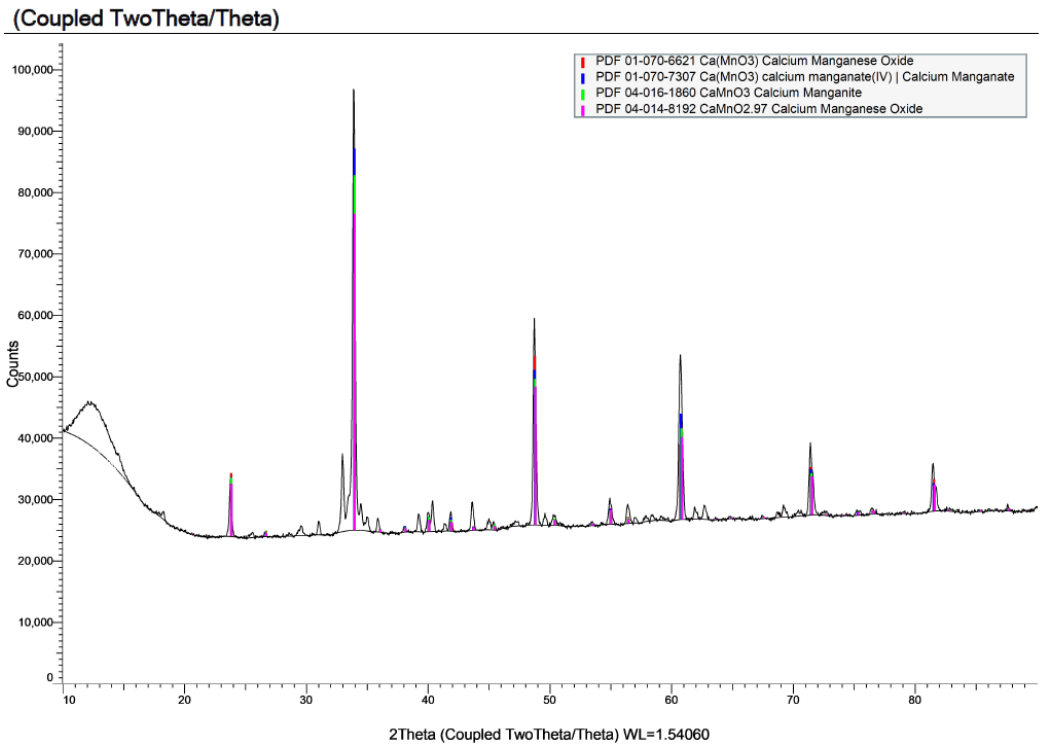

Figure 19: *X-ray diffraction analysis of Sample 1.10 showing peak matches with $CaMnO_{3-\delta}$ and related perovskite oxide phases*

7.2.2. Sample 2 – $CaFeO_{3-\delta}$

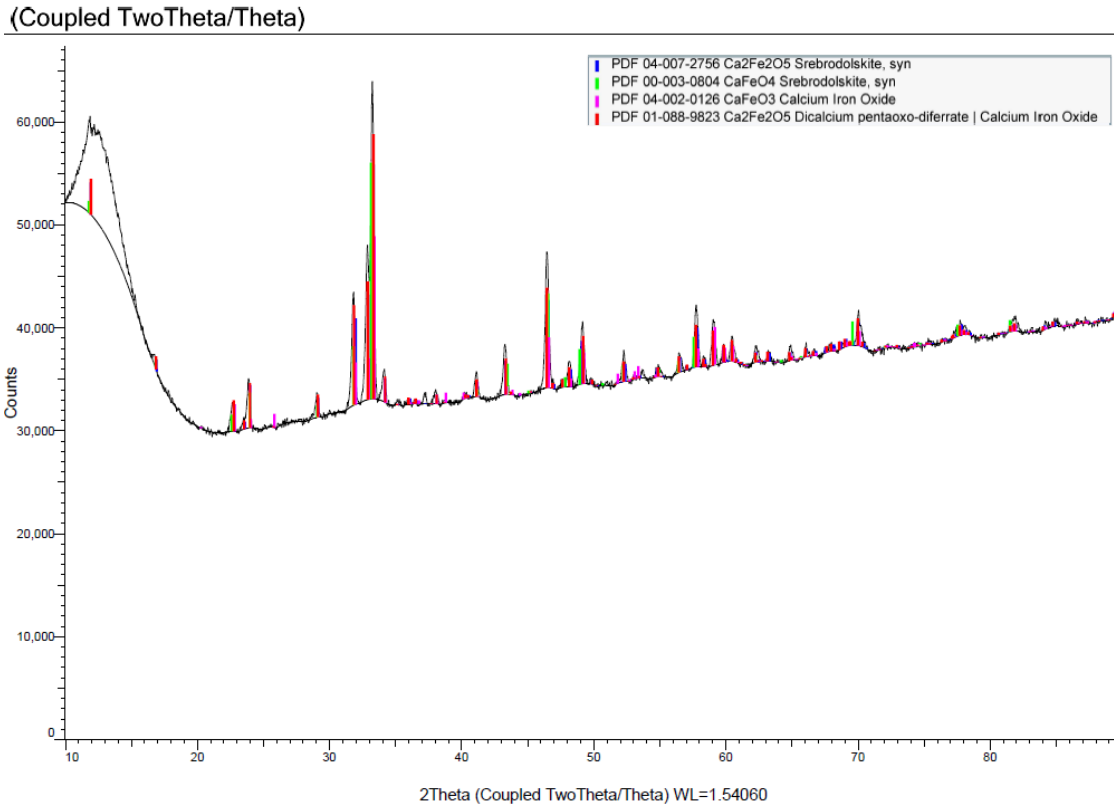

Figure 20: *X-ray diffraction analysis of Sample 2 showing peak matches with $CaFeO_{3-\delta}$ and related oxide phases*

7.2.3. Sample 3 – $LaMnO_{3-\delta}$

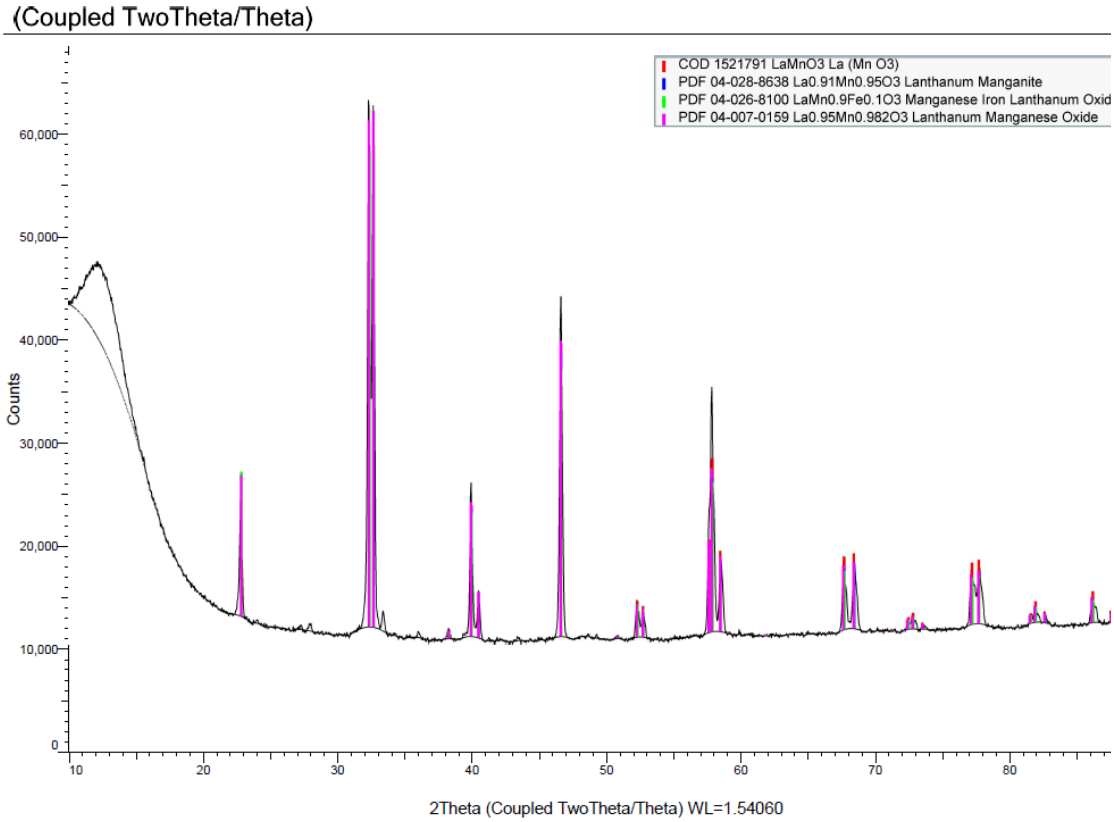

Figure 21: *X-ray diffraction analysis of Sample 3 showing peak matches with $LaMnO_{3-\delta}$ and related oxide phases*

7.2.4. Sample 4 – $LaFeO_{3-\delta}$

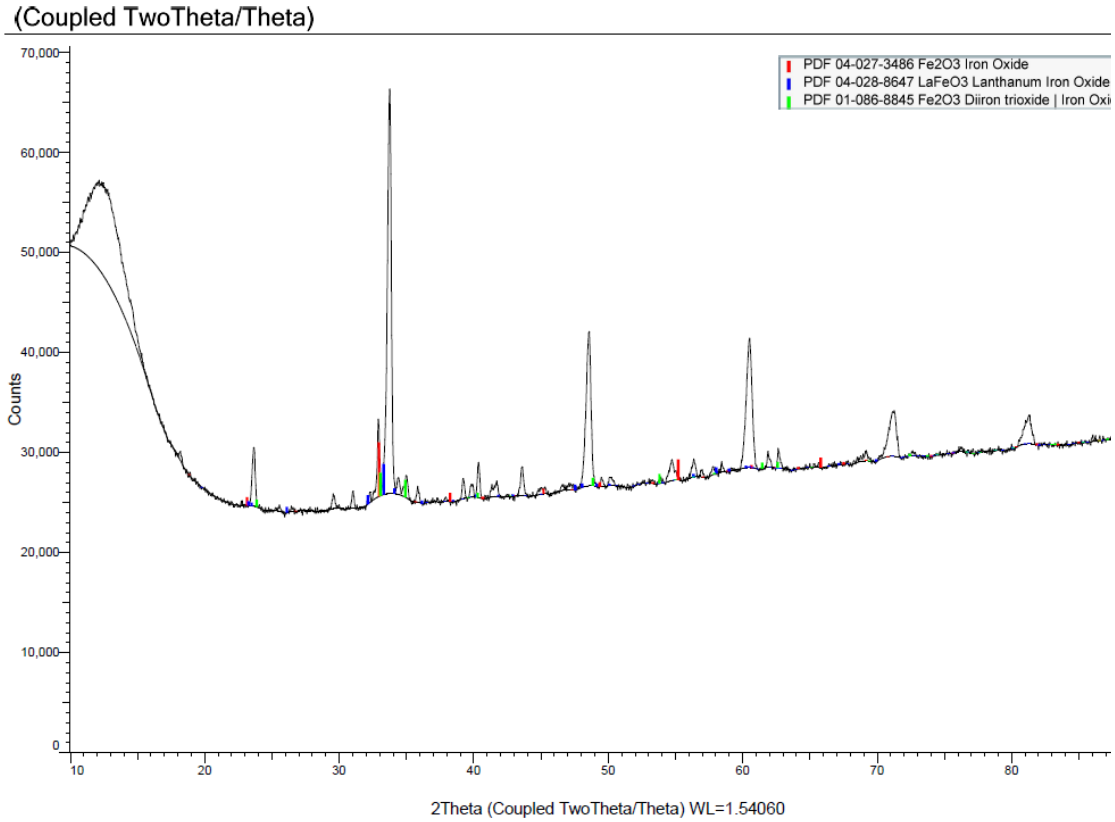

Figure 22: *X-ray diffraction analysis of Sample 4 showing peak matches with $LaFeO_{3-\delta}$ and related oxide phases*

7.2.5. Sample 5 – $CaFe_{0.2}Mn_{0.8}O_{3-\delta}$

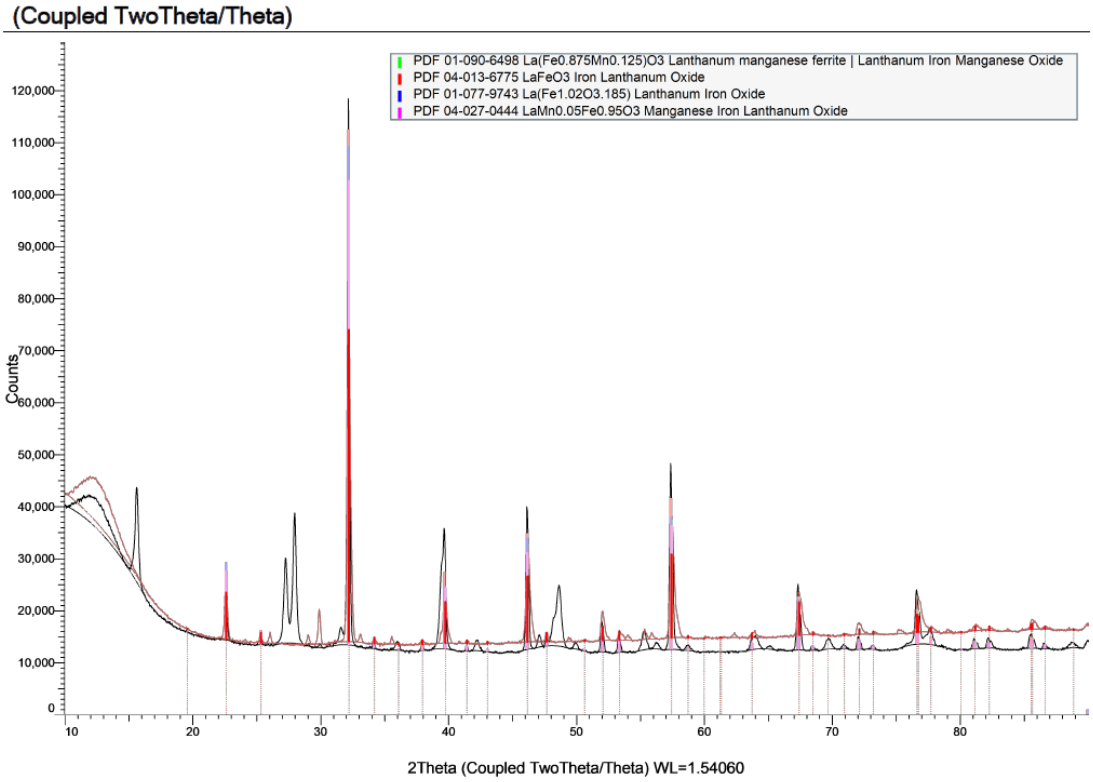

Figure 23: *Comparison of diffractograms showing evidence of a perovskite fraction in $CaFe_{0.2}Mn_{0.8}O_{3-\delta}$ (black line) based on its similarity to $LaFe_{0.8}Mn_{0.2}O_{3-\delta}$ (red line)*

7.2.6. Sample 6 – $CaFe_{0.8}Mn_{0.2}O_{3-\delta}$

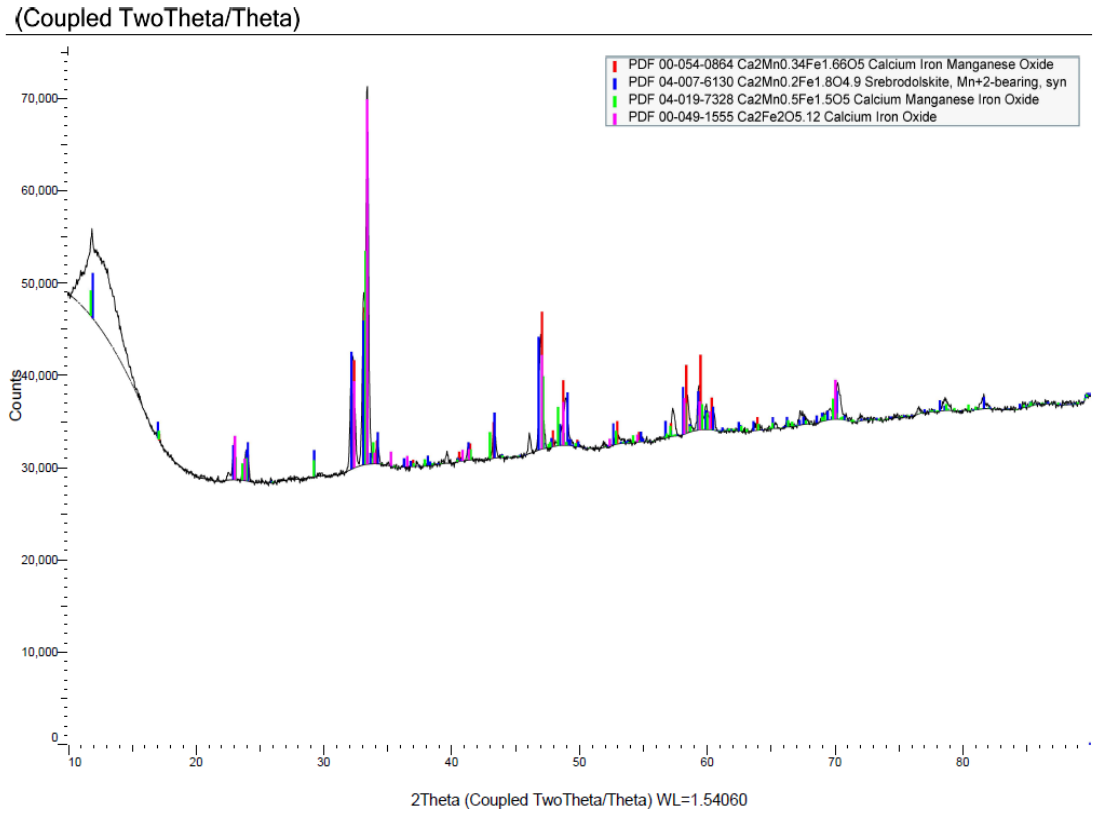

Figure 24: *X-ray diffraction analysis of Sample 6 showing peak matches*

7.2.7. Sample 7 – $CaFe_{0.5}Mn_{0.5}O_{3-\delta}$

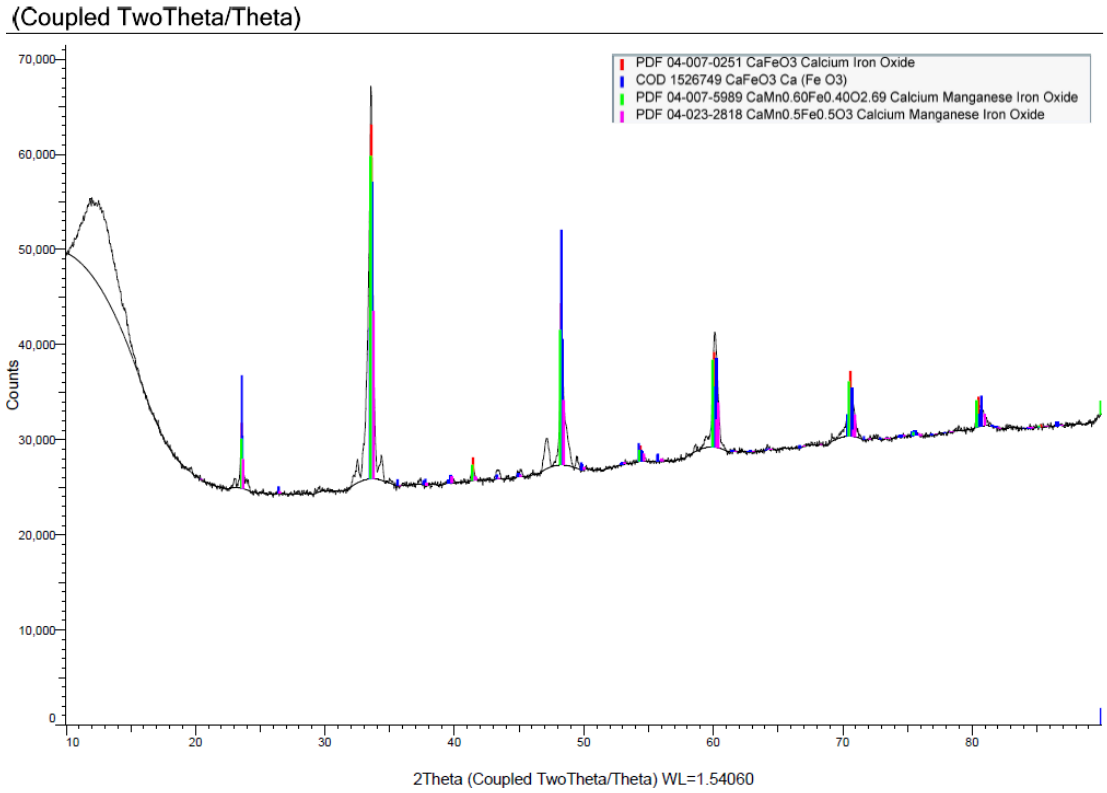

Figure 25: *X-ray diffraction analysis of Sample 7 showing peak matches*

7.2.8. Sample 8 – $LaFe_{0.2}Mn_{0.8}O_{3-\delta}$

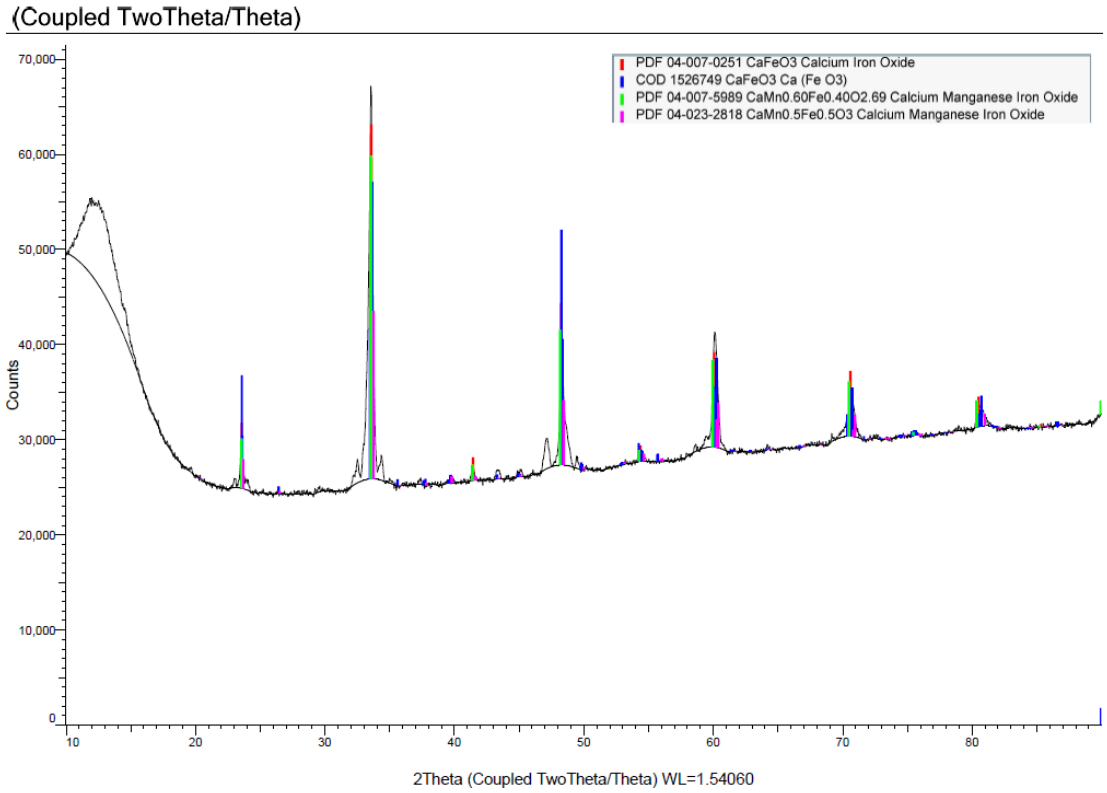

Figure 26: *X-ray diffraction analysis of Sample 8 showing peak matches*

7.2.9. Sample 9 – $LaFe_{0.8}Mn_{0.2}O_{3-\delta}$

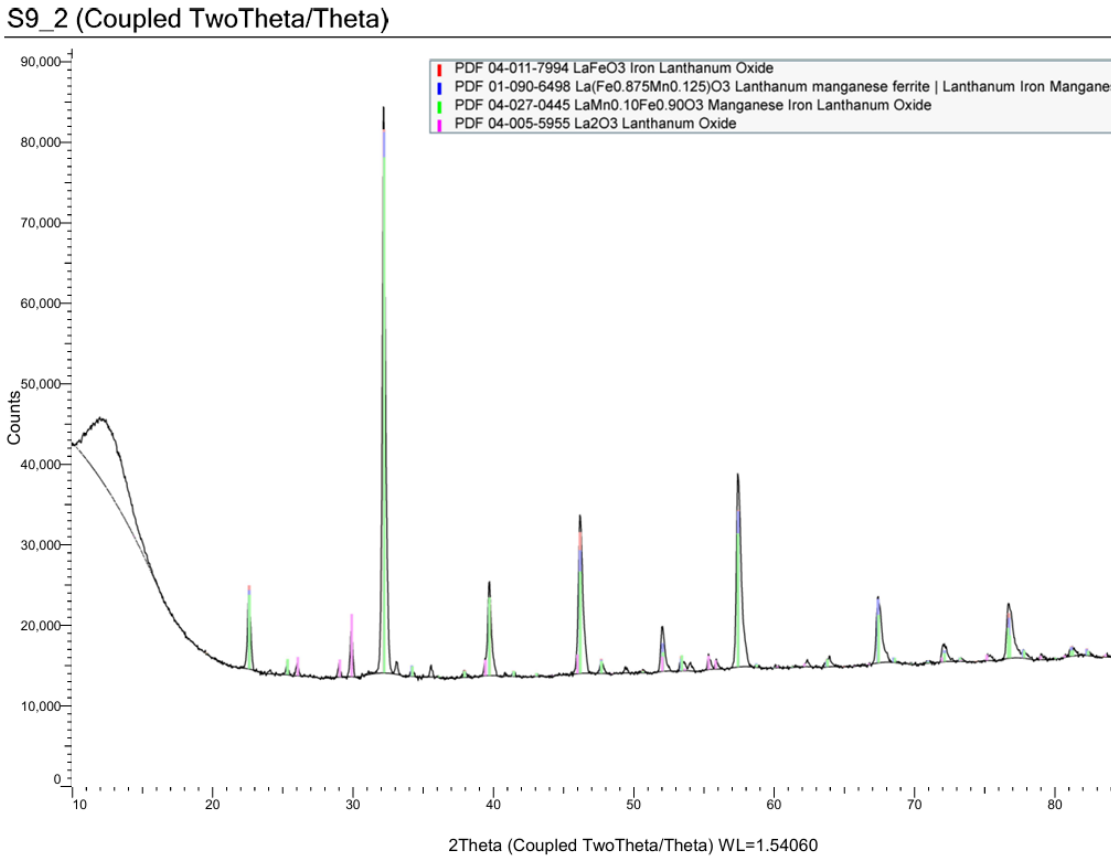

Figure 27: *X-ray diffraction analysis of Sample 9 showing peak matches*

7.2.10. Sample 10 – $LaFe_{0.5}Mn_{0.5}O_{3-\delta}$

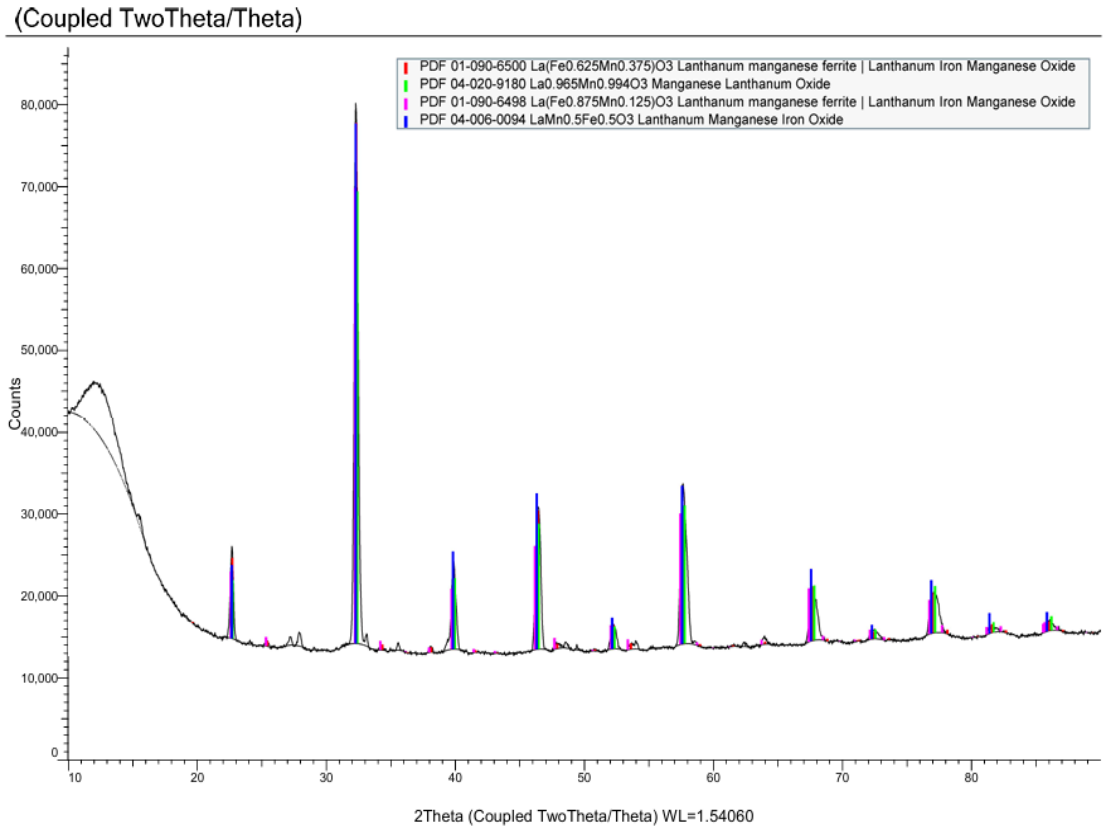

Figure 28: *X-ray diffraction analysis of Sample 10 showing peak matches*

7.2.11. Sample 11 – $Ca_{0.2}La_{0.8}FeO_{3-\delta}$

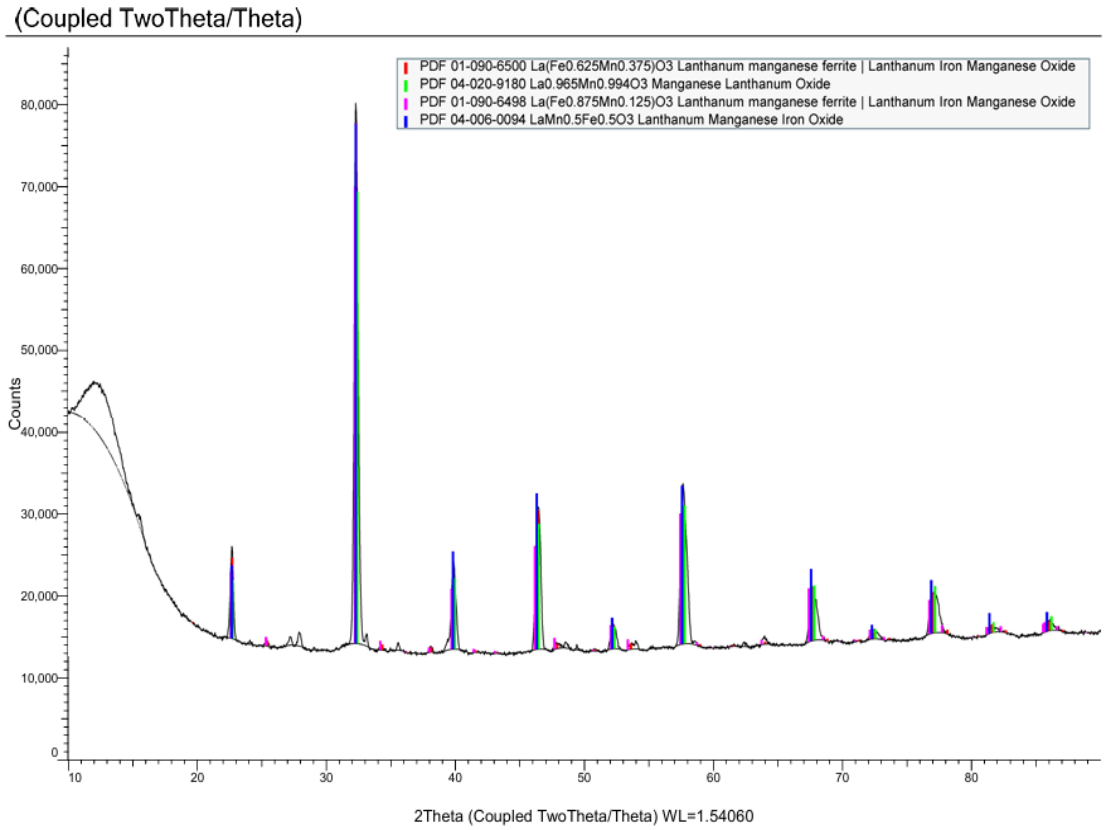

Figure 29: *X-ray diffraction analysis of Sample 11 showing peak matches*

7.2.12. Sample 12 – $Ca_{0.8}La_{0.2}FeO_{3-\delta}$

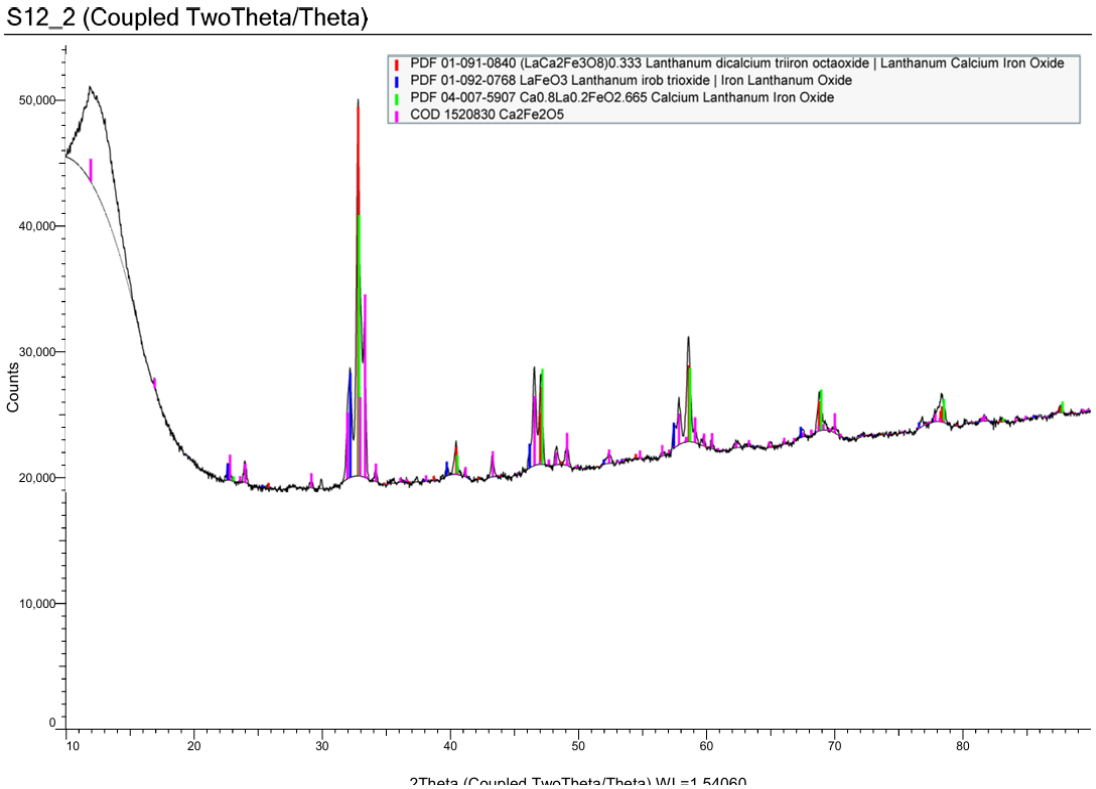

Figure 30: *X-ray diffraction analysis of Sample 12 showing peak matches*

7.2.13. Sample 13 – $Ca_{0.5}La_{0.5}FeO_{3-\delta}$

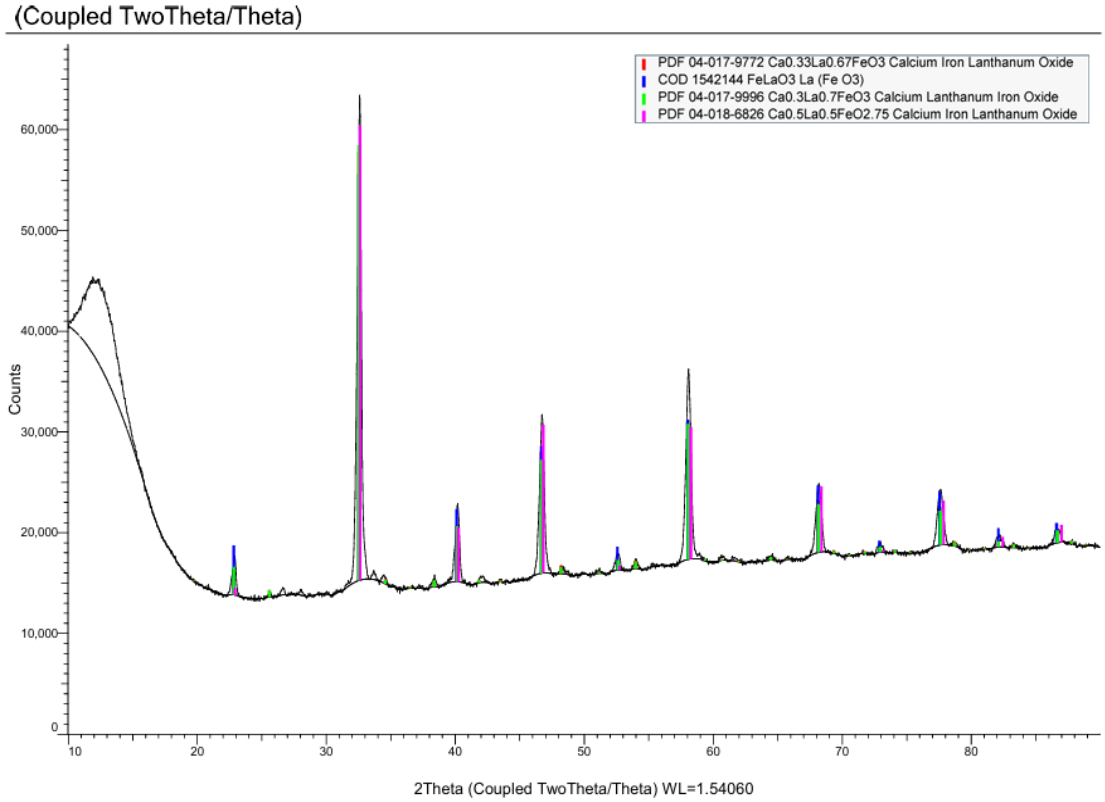

Figure 31: *X-ray diffraction analysis of Sample 13 showing peak matches*

7.3. Thermogravimetric analysis diagrams

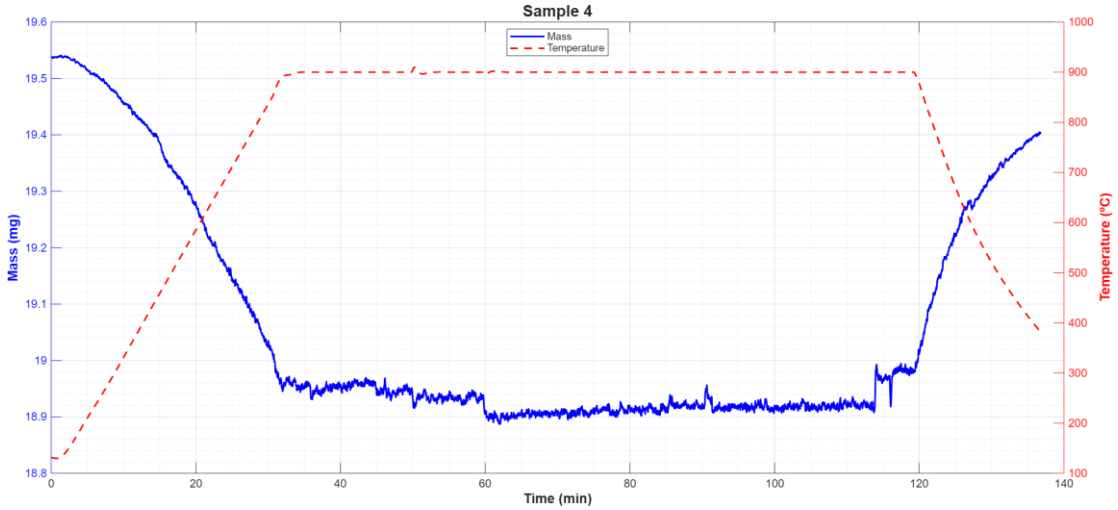

Figure 32: *Thermogravimetric profile of Sample 4 ($LaFeO_3$) during a CO reduction and CO_2 oxidation cycle at 900°C.*

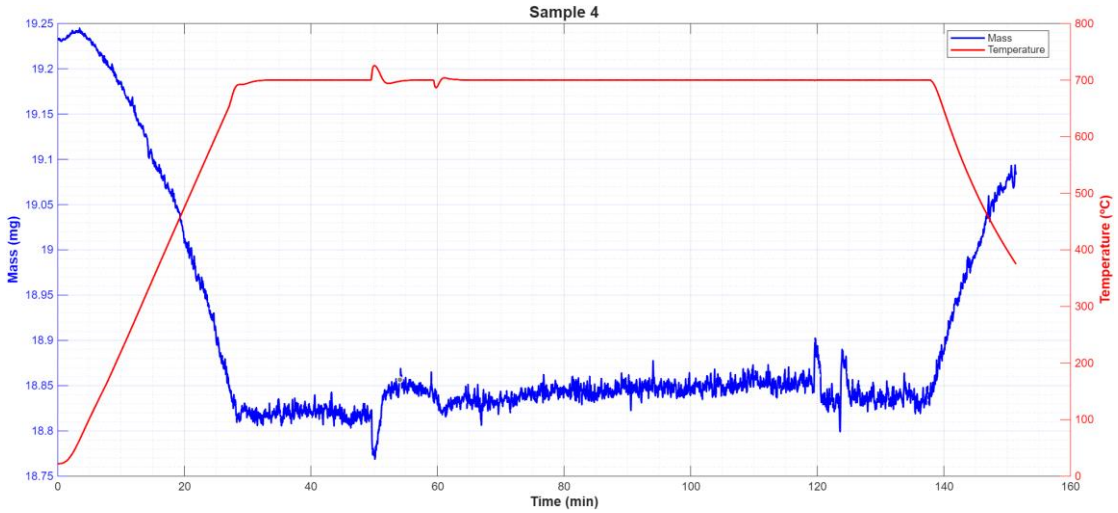

Figure 33: *Thermogravimetric profile of Sample 4 ($LaFeO_3$) during a CO reduction and CO_2 oxidation cycle at 700°C.*

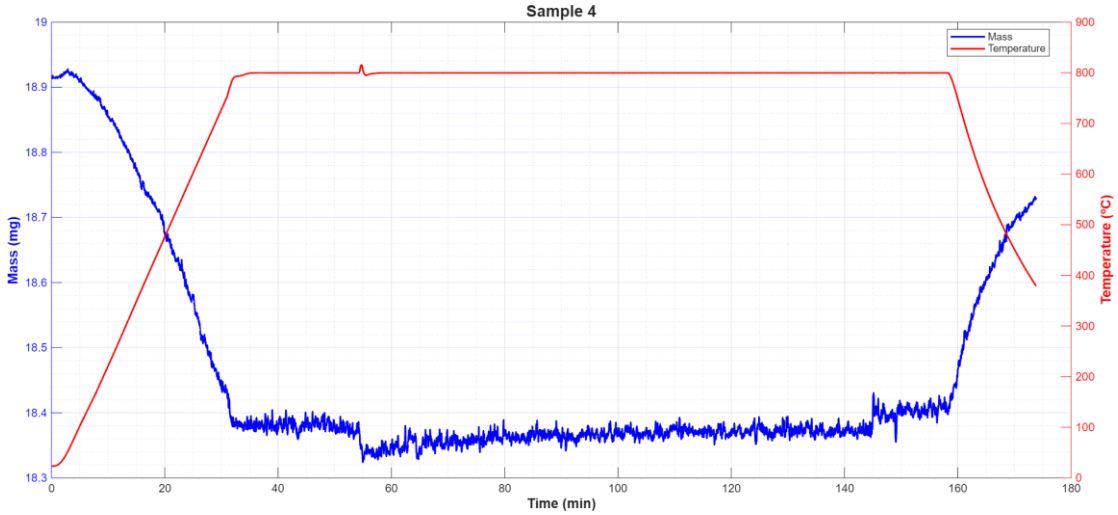

Figure 34: *Thermogravimetric profile of Sample 4 ($LaFeO_3$) during a CO reduction and CO_2 oxidation cycle at 800°C.*

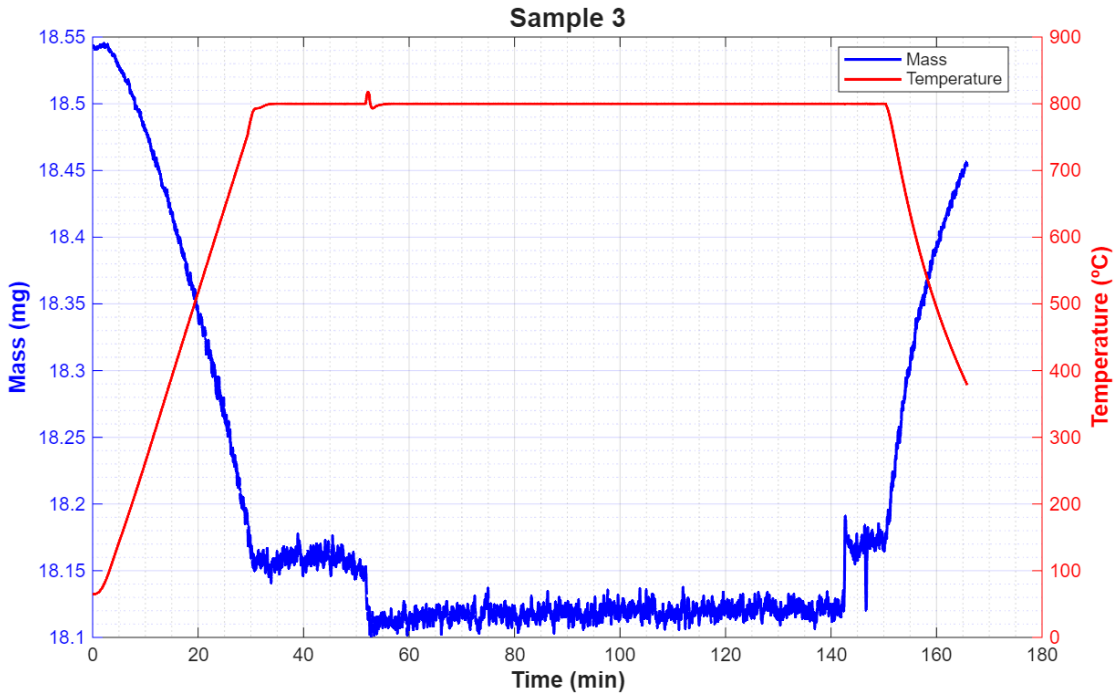

Figure 35: *Thermogravimetric profile of Sample 3 ($LaMnO_3$) during a CO reduction and CO_2 oxidation cycle at 800°C.*

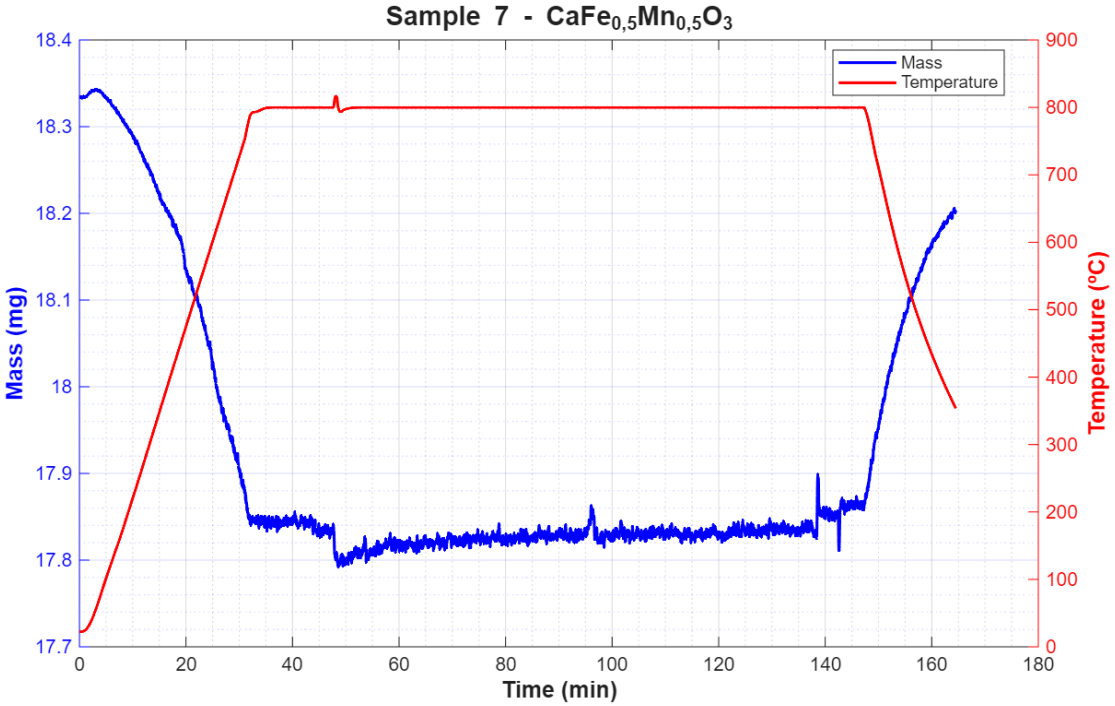

Figure 36: *Thermogravimetric profile of Sample 7 ($CaFe_{0.5}Mn_{0.5}O_3$) during a CO reduction and CO_2 oxidation cycle at 800°C.*

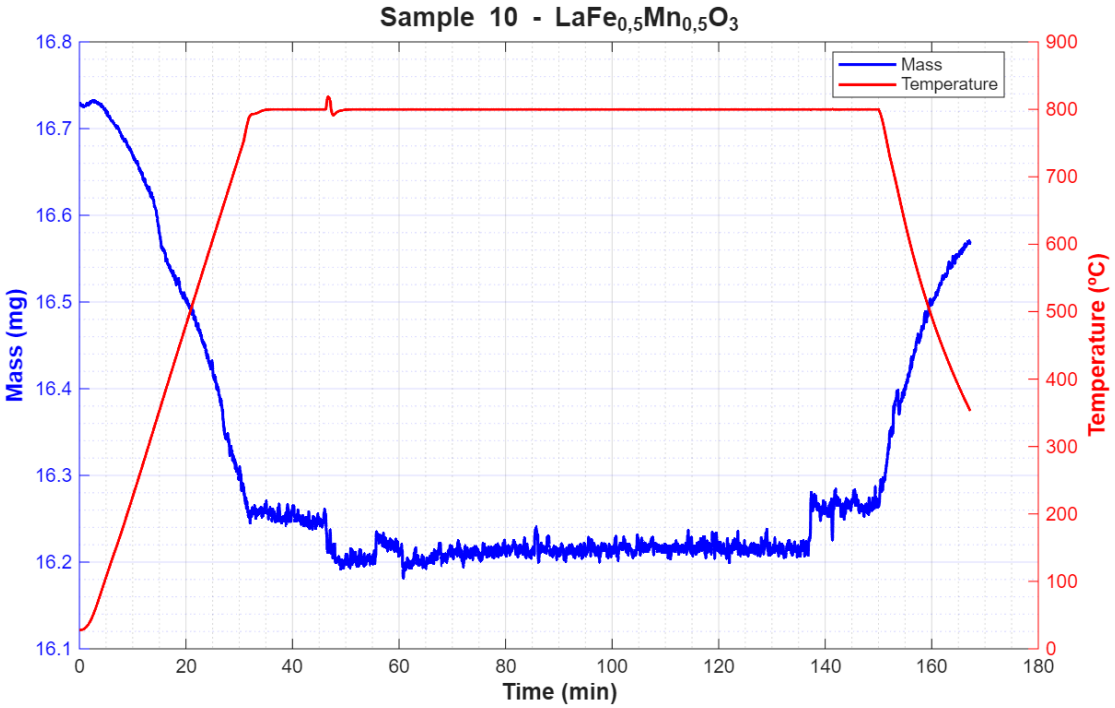

Figure 37: *Thermogravimetric profile of Sample 10 ($LaFe_{0.5}Mn_{0.5}O_3$) during a CO reduction and CO_2 oxidation cycle at 800°C.*

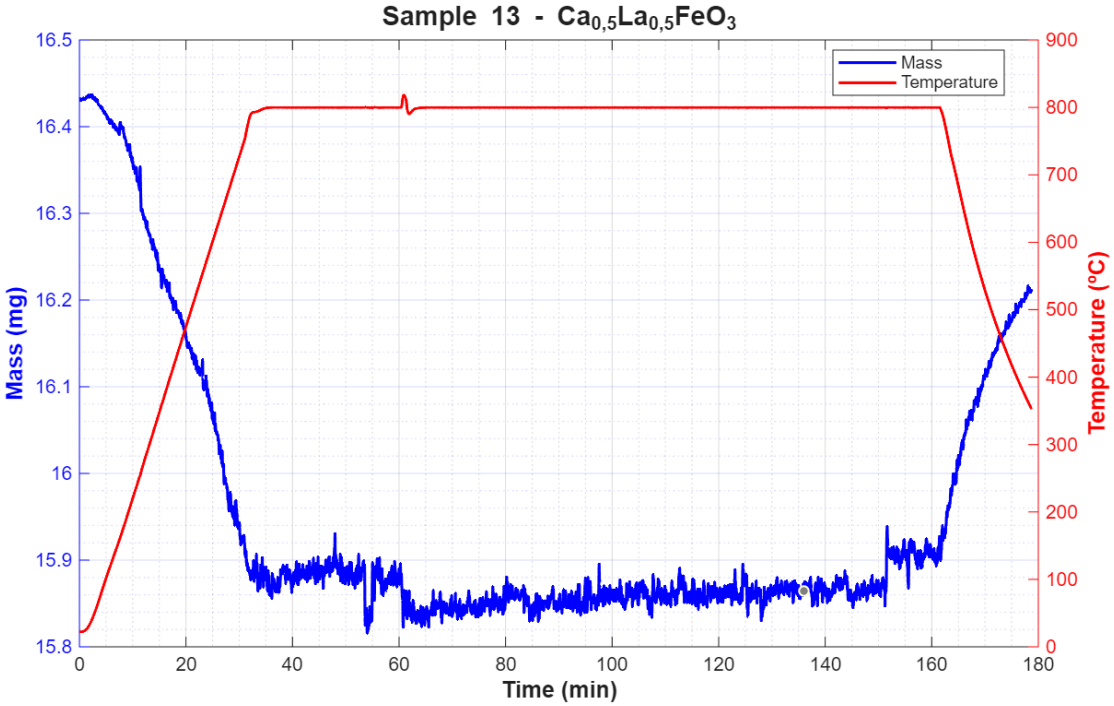

Figure 38: *Thermogravimetric profile of Sample 13 ($Ca_{0.5}La_{0.5}FeO_3$) during a CO reduction and CO_2 oxidation cycle at 800°C.*

DEPARTMENT OF SPACE, EARTH AND ENVIRONMENT
CHALMERS UNIVERSITY OF TECHNOLOGY
Gothenburg, Sweden 2026
www.chalmers.se

CHALMERS
UNIVERSITY OF TECHNOLOGY